Electric field dependence of pocket and nonpocket impurity gap modes in KI and the establishment of Ag^+ quadrupolar deformability

A. Rosenberg*
Laboratory of Atomic and Solid State Physics and Materials Science Center, Cornell University, Ithaca, New York 14853-2501

K. W. Sandusky
Department of Physics and Astronomy, Arizona State University, Tempe, Arizona 85287-1504

B. P. Clayman†
Laboratory of Atomic and Solid State Physics and Materials Science Center, Cornell University, Ithaca, New York 14853-2501

J. B. Page
Department of Physics and Astronomy, Arizona State University, Tempe, Arizona 85287-1504

A. J. Sievers
Laboratory of Atomic and Solid State Physics and Materials Science Center, Cornell University, Ithaca, New York 14853-2501
(Received 6 April 1995)

Far-infrared static electric field measurements have been made for a variety of KI point defects which produce vibrational modes in the pure crystal phonon gap. The extremely small field-induced frequency shifts ($\leqslant 0.02$ cm^{-1}) of the KI gap modes associated with anion impurities were accurately determined with a precision of ± 0.003 cm^{-1} by using a global analysis method. No frequency shifts were observed for the Rb^+ or Cs^+ gap modes, up to the maximum applied field of $\sim$100 kV/cm in the [100] direction. Most revealing are the field-induced frequency shifts for the pocket gap modes associated with the Ag^+ impurity, which are nearly two orders of magnitude smaller than the field-induced shifts measured for low-frequency Ag^+-induced resonant modes. The fact that the pocket-mode displacements are sharply peaked on the (200) family of ions renders them sensitive to the host-lattice anharmonicity near those sites, whereas the resonant modes probe the defect and its nearest neighbors. These *E*-field measurements and earlier stress-shift measurements are analyzed using a quasiharmonic perturbed shell model. In this approach the effect of either an applied stress or an applied *E* field is to move the equilibrium positions of the ions, thereby renormalizing the harmonic force constants via the local cubic and quartic anharmonicity. The two types of experiments produce local strains of orthogonal symmetries, and hence provide complementary information. The theoretical analysis of the *E* field and stress measurements allows us to establish firmly that the Ag^+ ion in KI possesses a significant electronic quadrupolar deformability. In turn, this finding strongly supports earlier suggestions that the silver ion quadrupolar deformability is an important feature in the dynamics of other host-silver defect systems and of the silver halides.

I. INTRODUCTION

Low concentrations of substitutional Ag^+ ions in KI produce an unusual impurity-induced vibrational spectrum that has been examined in some detail.[1–5] The observation that the entire $T=0$ K spectrum disappears upon heating to 25 K (Refs. 6–8) results from the Ag^+ ion moving from the on-center configuration to an as yet incompletely determined off-center position.[9] With increasing temperature, the ($T=0$ K) IR (Refs. 10 and 11) and Raman[7] resonant modes simply vanish, with a single distinguishing temperature dependence and with very little shifting or broadening. This behavior is quite different from that of systems exhibiting thermal instabilities driven by ''soft'' modes, whose frequencies approach zero with decreasing temperature.[12] Moreover, the observed rate at which the KI:Ag^+-induced vibrational spectra disappears is much faster than can be explained by population effects associated with the Ag^+ ion moving off center in a static anharmonic potential well, suggesting that the high-temperature configuration involves a large number of states of nearly the same energy as the on-center configuration.[6] This raises the question of the applicability of standard Lifshitz defect phonon theory,[13–15] which assumes a single, well-isolated, potential energy minimum.

Motivated by these experimental results, we have carried out a series of detailed experimental/theoretical investigations of the vibrational properties of this unusual point-defect system in the $T=0$ K *on-center* configuration.[7,8,16] Our theoretical approach has been to analyze the measured spectral properties by applying a perturbed shell model within the standard Lifshitz theory. Surprisingly, we find that, despite this system's highly anomalous thermal behavior, its $T=0$ K on-center dynamics are well described by a quasiharmonic defect model, which treats anharmonic effects as perturbations. However, the experimental/theoretical comparisons have revealed several unusual properties, including: (1) a class of impurity modes, called ''pocket'' gap modes, whose vibrational amplitudes are not peaked at the defect site but

 © 1996 The American Physical Society

rather are highly localized on host lattice ions well removed from the Ag^+;[8,17] (2) anomalous stress-induced frequency shifts measured for the pocket modes;[16] (3) small dc E-field-induced frequency shifts for the pocket modes, which were briefly described in a letter[18] and are discussed in detail here. The addition of the E-field measurements and their theoretical analysis demonstrate that the Ag^+ ion in KI possesses a significant electronic quadrupolar deformability. This has important implications for the dynamics of Ag^+ in other systems.

Aspects of our preceding studies are relevant to the present E-field work. (1) Despite the thermal instability, the spectral features associated with the $T=0$ K on-center vibrational dynamics of KI:Ag^+ are well described by a perturbed *harmonic* shell model.[7] A striking prediction of this model is the existence of three very nearly degenerate local modes with frequencies in the host KI phonon gap. These gap modes are of three different symmetries, and their frequencies are equal to within 2%. (2) Their predicted displacement patterns are also very unusual in being strongly peaked on the defect's fourth-nearest-neighbor sites $[(\pm 200), (0\pm 20),(00\pm 2)]$, with the displacements of the defect and its nearest neighbors more than an order of magnitude smaller than that of the fourth-nearest neighbors. In sharp contrast, the displacement patterns found for standard impurity-induced localized modes are peaked on the defect or its nearest neighbors.[14,15,19] (3) In Refs. 8 and 17 we showed that the natural occurrence of a 7% isotopic abundance of $^{41}K^+$ isotopes in the KI host strongly mixes these nearly degenerate pocket gap modes, producing an IR-active isotope gap mode with a predicted frequency shift and relative absorption strength in good agreement with the shift and strength measured in subsequent IR experiments. This agreement between theoretical predictions and experiment, combined with the failure of alternative explanations for the experimental results, provided a direct confirmation of the existence of the nearly degenerate pocket gap modes and their very unusual displacement patterns.

To probe the anharmonicity associated with the KI:Ag^+ on-center configuration, we built upon these results by undertaking studies of uniaxial stress[16] and dc electric-field-induced frequency shifts,[18] both for the pocket modes, and for the low-lying impurity-induced resonant modes[3,5] that exist below 20 cm^{-1}. The fact that the pocket-mode displacements are sharply peaked on the (200) family of host ions renders the pocket modes sensitive to the host-lattice anharmonicity near those sites, whereas the resonant modes probe the defect and its nearest neighbors. Within a quasiharmonic approach, which treats the anharmonicity perturbatively, the effect of either applied stress or an applied E field is to move the equilibrium positions of the ions, thereby renormalizing the harmonic force constants via the local cubic and quartic anharmonicity. The two types of experiments produce local strains of orthogonal symmetries and hence provide complementary information. Our approach to the data is to use a quasiharmonic extension of our perturbed harmonic shell model to fit the measured pocket-mode stress shifts and then use the stress-fit anharmonicities to predict the pocket-mode dc E-field-induced frequency shifts. We find that our original model[7] predicts E-field-induced shifts that are nearly two orders of magnitude larger than the observed shifts. However, with the addition of Ag^+ electronic quadrupolar deformability (QD) to the original perturbed harmonic shell model, the predicted dc E-field-induced pocket-gap-mode frequency shifts are in good agreement with the experimental results. In addition, this model also substantially improves other predictions of our earlier harmonic model, as well as reproducing the measured dc E-field-induced frequency shifts of the KI:Ag^+ low-frequency *resonant* modes, whose measured E-field shifts are nearly two orders of magnitude larger than those for the pocket modes.

Besides the Ag^+ QD, another important feature of the model is its inclusion of relaxation-induced nearest-neighbor force-constant changes *beyond* the defect's fourth-nearest neighbors; these changes can be computed without the addition of any new parameters beyond those contained in the original harmonic model.[20] Hence, the many improvements of the QD model result from the addition of a single parameter to the earlier model. In this paper we will also consider several alternative models using other force-constant changes and show that these models fail badly. Thus, based upon the successes of the QD model and the failures of the alternative models, we conclude that extended defect-induced relaxations and the Ag^+ QD play an essential role in determining the KI:Ag^+ on-center dynamics. Our results strongly support earlier speculations that the Ag^+ QD is an important feature in the dynamics of other host-silver defect systems and of the silver halides,[21–27] including the superionic conductivity observed in AgI.[25]

Experimental details are provided in the next section. First, the electric-field apparatus is described, and then the experimental results for the Stark effect in KI:Ag^+ and KI:Cl^- are presented, followed by data analysis. For comparison, the E-field results for gap modes of several other impurities in KI are included. Section III focuses on the theoretical aspects of the work: First, our original force-constant change model is compared with the data and shown to be inadequate. The QD model is then developed in a stepwise manner and the predicted pocket-mode shifts and mixing are shown to agree with experiment. Finally, the experimentally observed E-field-induced mixing and shifts of the low-frequency resonant modes are compared with the predictions of this model and found to be in agreement. The similarities and differences between the results for the various gap modes are discussed in Sec. IV. General results and implications of the QD model are presented in the conclusion. The Appendix discusses the E-field-shift theory.

II. EXPERIMENT

Far-IR spectra of KI crystals doped with Ag^+ and other impurities were obtained with a fast-scan Fourier-transform spectrometer at resolutions between 0.1 and 0.5 cm^{-1}. A commercial optical-access liquid-He immersion cryostat with homemade polypropylene and/or Mylar film windows[16] was used to cool the samples. A homemade sample insert allowed the application of a dc E field to the samples during the measurements, with the incident far-IR radiation polarized either parallel or perpendicular to the applied dc E-field direction (i.e., $E_{IR}\|E_{dc}$ or $E_{IR}\perp E_{dc}$).

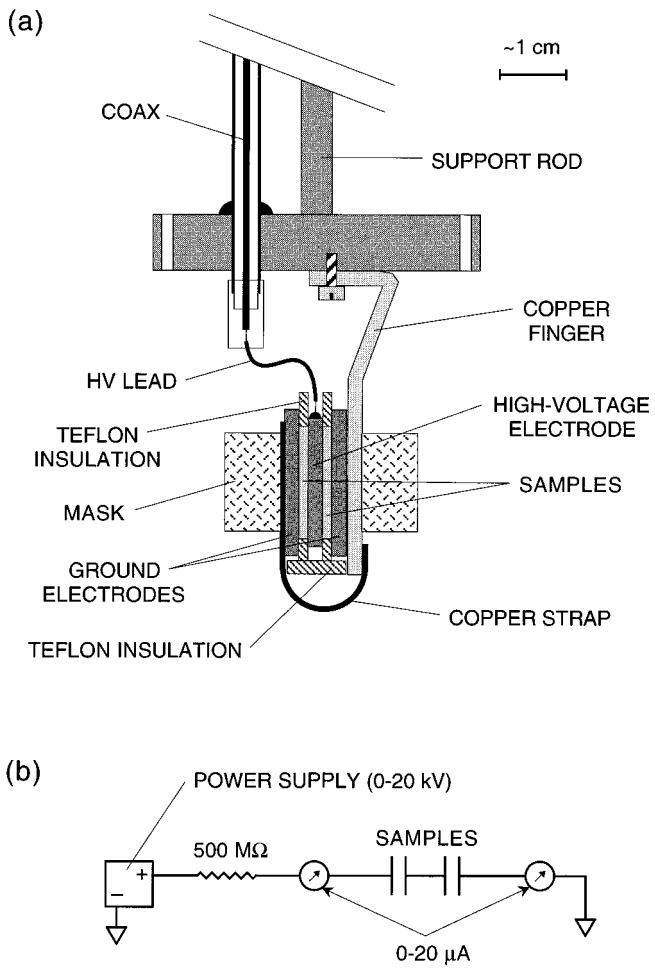

FIG. 1. Cryostat insert used for measuring the transmission of samples under an applied dc E field. (a) Expanded view of the sample holder. The thin copper-sheet strap provides electrical contact to the ground electrode away from the copper finger. The high-voltage lead is made of thin teflon-coated single-conductor wire. Pieces of teflon sheet ~1 mm thick are used to fill the gaps between the electrodes left by the samples as well as other areas where the high-voltage lead passes near ground potential. The propagation direction of the far-IR radiation is perpendicular to the plane of the page in this view. The mask, made of thin electrical tape and aluminum foil, prevents radiation not passing through the samples from reaching the detector. (b) Circuit diagram. In case of breakdown of the samples, the 500 MΩ resistor limits the current, which is monitored with the two micro-ammeters.

A. Experimental techniques

The cryostat sample insert for the far-IR E-field measurements is shown schematically in Fig. 1. Contact between a high-voltage dc power supply and an electrode sandwiched between two identical samples was made through a stainless-steel covered coaxial conductor containing teflon insulation; on opposite sides of the samples were grounded electrodes. The flange which sealed the top of the cryostat was provided with several compression o-ring feedthroughs permitting adjustment of the vertical position of the samples inside the cryostat without allowing air into the cold sample section. The samples could be immersed in either liquid or gaseous He. Since very low electric fields break down gaseous He, especially at the reduced pressure present in the cryostat, measurements could only be carried out in liquid. Although it was reported[5] that up to 50% higher fields could be obtained in normal liquid He than in superfluid He, the present cryostat was such that the normal liquid-He bubbles would scatter the incident far-IR radiation and add unacceptable noise to the spectra. Therefore, all measurements reported here were performed in superfluid He at applied fields of up to ~100 kV/cm.

The samples used for measurements with E_{dc} along the [100] crystallographic direction consisted of slabs, cleaved to a thickness of ~1 mm along the direction of the applied field, from boules grown by the Czochralski method at the Cornell Materials Science Center's Crystal Growing Facility. The sample length, along the direction of propagation of the far-IR radiation, typically was ~0.75 cm, but very short samples (~1.5 mm long) were measured in some cases. The third dimension (perpendicular to both the propagation and E-field directions) was ~1 cm. The samples used with E_{dc} along the [110] direction were cut into similarly sized shapes with a diamond string saw. The faces perpendicular to the propagation direction were ''wedged'' to avoid interference effects in the spectra; these faces plus the sample holder (electrodes plus mask; see Fig. 1) acted as an aperture for the far-IR radiation. All the KI:Ag^+ samples were heated to ~200 °C prior to the measurements in order to maximize the absorption strengths of the KI:Ag^+ modes, as described previously.[28]

The electrodes shown in Fig. 1 were plates of stainless steel, ~1.5 mm thick, which had been mechanically and electrochemically polished and had the corners and edges rounded by grinding. These precautions were taken to reduce the likelihood of electrical breakdown. The samples and the electrodes were held in place by tightly wrapping the whole assembly, above and below the samples, with thin low-temperature electrical tape. The uniformity of the field across the samples was enhanced by making the samples smaller than the electrodes and placing the samples in the centers of the electrodes; this differs from the technique described in Ref. 29. Teflon insulation was inserted wherever high-voltage areas were in proximity to grounded parts of the sample holder, as shown. Finally, a mask made of electrical tape and aluminum foil was attached to the outside surfaces of the ground electrodes to block any incident radiation not passing through the samples from reaching the detector. Additional details of the sample holder construction can be found in Ref. 30.

Even with the samples submerged in liquid He, the maximum field could only be maintained for a limited amount of time (ranging from minutes to hours, depending on the sample), after which intermittent breakdown began; once started, this breakdown could *not* be stopped by lowering the field and eventually led to the destruction of the samples. The heat released during the breakdown produced bubbles in the liquid helium, which shocked the samples, mechanically damaging them. Therefore, measurements were generally performed at low-field strengths first, with the maximum being reached gradually.

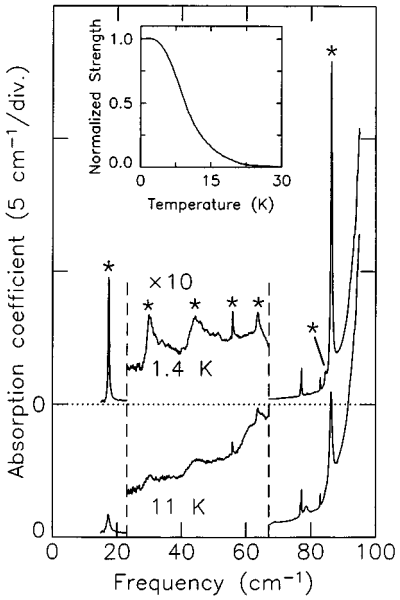

FIG. 2. Absorption coefficient of KI+0.4 mole % AgI below the reststrahl region of KI, at 1.4 K (upper trace) and 11 K (lower trace). The resolution is 0.1 cm^{-1}. The two spectra are displaced by a division on the ordinate axis for clarity; also, the ordinate scale in the region between 25 and 75 cm^{-1} has been expanded 10× to show the weak modes in the acoustic-phonon region. Asterisks identify the low-temperature modes associated with KI:Ag$^+$. These spectra are similar to those of Ref. 6, but at higher resolution. The dominant features are the KI:Ag$^+$ gap and resonant modes at 86.2 and 17.3 cm^{-1}, respectively; additional features are identified in the text. The inset shows the temperature dependence of the strengths of the KI:Ag$^+$ features (after Ref. 8).

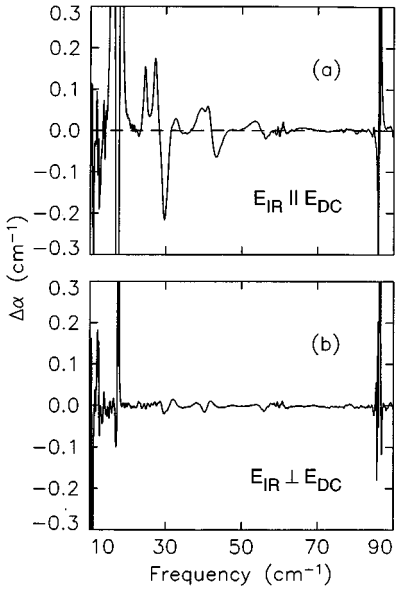

FIG. 3. Changes in the absorption of KI+0.1 mole % AgI below the reststrahl region of KI, induced by a [100] E field of 77 kV/cm. The resolution is 0.3 cm^{-1} and the temperature is 1.4 K. (a) $E_{IR} \| E_{dc}$. (b) $E_{IR} \perp E_{dc}$. The region below 50 cm^{-1} should be compared to Fig. 2 of Ref. 5. The sharp ''wiggles'' near 60 cm^{-1} are probably due to 60 Hz pickup in the high-voltage power supply and leads. Note that the absorption of the resonant and gap modes at 17.3 and 86.2 cm^{-1}, respectively, is nearly saturated in this sample.

B. Errors

The statistical error associated with the shift at each value of the applied E field was determined from several independent measurements of the shift at that field. These measurements consisted of repeated cycling of the field between that E-field value and zero, and measuring the line shape with the field on and the field off for each such cycle. In addition, for each mode studied, such data were generally obtained on several samples. Systematic errors were not included; they were considered to be negligible based on a comparison with previous E-field results.[4,5] For the linear fits to the plots of shift vs the square of the E field, the errors in the slopes were determined by the linear regression algorithm from the scatter in the data points; these slope errors were propagated through the equations relating the slopes to the E-field coupling coefficients to determine the errors in the latter.

C. Results for KI:Ag$^+$ and KI:Cl$^-$

Before presenting the new E-field results, we first describe the low-temperature absorption spectrum of KI:Ag$^+$ in the absence of an applied E field, below the reststrahl region of KI. A detailed discussion of this spectrum has been given in Refs. 6, 8, and 17. As shown in Fig. 2, the substitutional Ag$^+$ defect gives rise to two strong localized modes: a resonant mode in the acoustic phonon region, at 17.3 cm^{-1}, and a gap mode in the region between the acoustic and optic phonons, at 86.2 cm^{-1}. Additional weak features due to Ag$^+$ at 30, 44, 55.8, and 63.6 cm^{-1} (in the KI acoustic-phonon region), and at 84.5 cm^{-1} (in the KI gap region) caused by $^{39}K^+ \rightarrow {}^{41}K^+$ host-lattice isotopic substitution,[8] are also visible in the lower-temperature (1.4 K) spectrum. Small concentrations of other naturally occurring impurities in these crystals give rise to additional gap modes, at 76.8 and 77.1 cm^{-1} due to Cl$^-$ and at 82.9 cm^{-1} due to Cs$^+$ (and another at 78.9 cm^{-1}, of unknown origin). In the higher-temperature spectrum of Fig. 2 (11 K), all of the Ag$^+$ features are weaker, while the strengths of features associated with other defects (e.g., Cl$^-$ and Cs$^+$) remain unchanged; in addition, new features associated with the Ag$^+$ defects appear at 69 and 78.6 cm^{-1}. The inset of Fig. 2 shows the ''universal'' temperature dependence of the strengths of the KI:Ag$^+$ low-temperature configuration features, including the strong resonant and gap modes (after Ref. 6).

The E-field-induced changes in the acoustic phonon region of KI:Ag$^+$ have been studied in detail previously.[4,5] Our results for an applied [100] dc E field, covering the entire spectral region below the KI reststrahl region, are shown in Fig. 3. Here, as elsewhere in this paper, the change in the absorption coefficient α induced by the dc E field is given as $\Delta\alpha \equiv \alpha(\text{field on}) - \alpha(\text{field off})$. The results in the acoustic-phonon region, including the shift of the T_{1u}-symmetry IR-active resonant mode and the field-induced IR activity of a lower-frequency E_g-symmetry Raman-active resonant mode, are very similar to those in Fig. 2 of Ref. 5 (which were obtained at a higher field). The higher resolution of the present data reveals additional detail, such as the splitting of the broad field-induced mode at 25 cm^{-1} in Ref. 5 into two sharper modes at 25 and 28 cm^{-1}, the narrower linewidth of

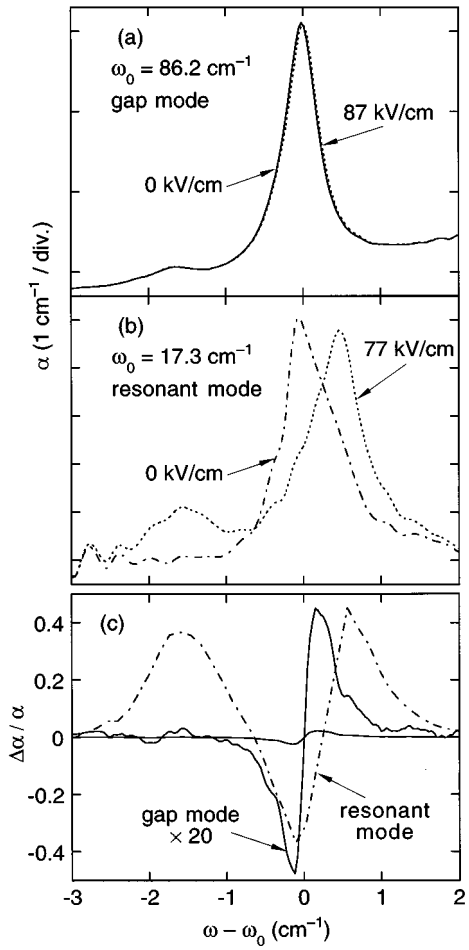

FIG. 4. E-field-induced shifts of the KI:Ag^+ (a) gap and (b) resonant modes for $E_{IR}\|E_{dc}$ [100] at 1.4 K; each spectrum is displaced along the abscissa by the frequency of the mode, ω_0, for clarity. (a) Gap mode region of KI+0.04 mole % AgI at 0.1 cm^{-1} resolution, ω_0=86.2 cm^{-1}. Solid line: zero field, dotted line: 87 kV/cm. (b) Resonant mode region of KI+0.1 mole % AgI at 0.3 cm^{-1} resolution, ω_0=17.3 cm^{-1}. Dash-dotted line: zero field, dotted line: 77 kV/cm. (c) Comparison of the gap and resonant mode regions; $\Delta\alpha/\alpha \equiv [\alpha(\text{field on}) - \alpha(\text{field off})]/\alpha(\text{field off})$. Solid line: gap mode region, dash-dotted line: resonant mode region. An expanded (20×) version of the gap mode data is also shown.

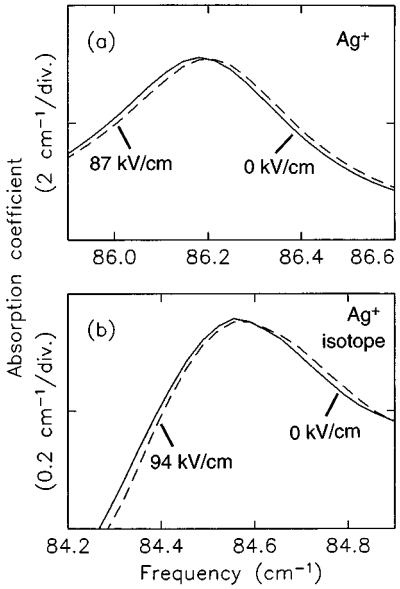

FIG. 5. Spectra of the KI:Ag^+ pocket gap modes with *no* applied E field (solid lines) and with an applied [100] E field (dashed lines), for $E_{IR}\|E_{dc}$. The resolution is 0.1 cm^{-1} and the temperature is 1.4 K; the nominal sample composition is KI+0.04 mole % AgI. (a) The 86.2 cm^{-1} main pocket gap mode at 87 kV/cm. (b) The 84.5 cm^{-1} isotope pocket gap mode at 94 kV/cm. Note that the ordinate scale in (b) is expanded 10× relative to that in (a).

the field-induced feature at 30 cm^{-1}, and additional weak features at 53.5 and 55 cm^{-1}, just above the upper limit of the spectral region studied previously.[5] In addition, as seen in Fig. 3(b), weak spectral changes are observed for $E_{IR}\perp E_{dc}$, where *no* changes were reported previously;[5] it is *not* likely that the latter are artifacts of imperfect polarization since they do not correspond directly to features in the $E_{IR}\|E_{dc}$ spectrum of Fig. 3(a).

Prior to the results presented in this paper, none of the previous E-field studies, including those of the KI:Ag^+ modes[4,5] as well as those of activated modes due to various other lattice-defect systems,[19,29,31–33] extended to high enough frequency to examine the effect of an applied E field on gap modes. Although the main focus of the present study is on the gap modes due to Ag^+, we have also measured the E-field dependence of gap modes due to other lattice-defect systems for purposes of comparison to the Ag^+ results. In particular, since Cl^- is typically present as a natural impurity in pure KI and gives rise to gap modes whose structure has been carefully analyzed previously,[34] we have studied in some detail the E-field dependence of the KI:Cl^- gap modes. Note that a similar comparison between the Ag^+ and Cl^- gap modes in KI was carried out in our previous uniaxial stress study.[16]

Extremely small E-field-induced shifts in the positions of the KI:Ag^+ gap modes are observed. The disparity between the shift of the main gap mode at 86.2 cm^{-1} and that of the resonant mode at 17.3 cm^{-1} is brought out clearly in Fig. 4, where the spectra are displaced along the abscissa to facilitate the comparison. Note that these shifts of the gap modes correspond to the *maximum* applied field with $E_{IR}\|E_{dc}$[100] (which gives rise to the largest effects). The small size of the gap-mode shift in Fig. 4(a) makes the line shape under the maximum applied field nearly indistinguishable from the zero-field line shape; by contrast, the much larger shift of the resonant mode is apparent in Fig. 4(b). The normalized field-induced changes in the absorption coefficient for the gap and resonant modes of KI:Ag^+ are shown in Fig. 4(c); in order to plot both spectral regions on the same ordinate axes, the gap mode curve in Fig. 4(c) was expanded 20×, as indicated. The appearance of a field-activated resonant mode just below the 17.3 cm^{-1} IR-active resonant mode, discussed in Ref. 5, is evident in Fig. 4(b) and (c); no such field-activated modes are observed in the gap mode region.

Since the KI:Ag^+ gap mode line shapes in Fig. 4(a) are nearly indistinguishable, the line shapes of the main and isotope gap modes of KI:Ag^+, with and without an applied E field, are displayed on expanded scales in Fig. 5. This figure clearly shows that the small shifts of these two pocket modes

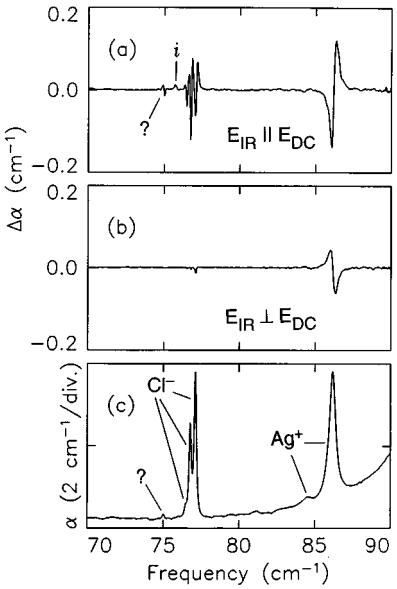

FIG. 6. Changes in the absorption coefficient of KI+0.04 mole % AgI induced by a [100] E field of 87 kV/cm. The resolution is 0.1 cm^{-1} and the temperature is 1.4 K. (a) $E_{IR} \| E_{dc}$. (b) $E_{IR} \perp E_{dc}$. (c) The corresponding spectrum at zero applied field. This spectral region shows both the KI:Ag^+ (84.5 and 86.2 cm^{-1}) and KI:Cl^- (77.1, 76.8, and 76.5 cm^{-1}) gap modes, for comparison; in addition, as seen in (a), for $E_{IR} \| E_{dc}$ a weak field-induced mode (marked i) appears at 75.7 cm^{-1}, just below the Cl^- modes, and another weak unidentified mode at 75 cm^{-1} [also seen in (c)] shifts with field in a direction *opposite* to that of the stronger Ag^+ and Cl^- gap modes.

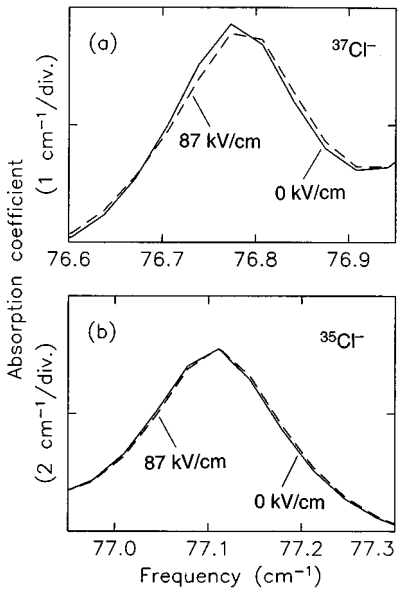

FIG. 7. Spectra of the KI:Cl^- gap modes with *no* applied E field (solid lines) and with an applied [100] E field (dashed lines) of 87 kV/cm, for $E_{IR} \| E_{dc}$. The resolution is 0.1 cm^{-1} and the temperature is 1.4 K; the nominal sample composition is KI+0.04 mole % AgI, and the Cl^- is present as a natural impurity. (a) The 76.8 cm^{-1} $^{37}Cl^-$ gap mode. (b) The 77.1 cm^{-1} $^{35}Cl^-$ gap mode. Note that the ordinate scale in (a) is expanded 2× relative to that in (b).

are ''rigid'' (in the sense that no field-induced changes in the strengths of these modes are observed at this value of field) and comparable in size.

The corresponding field-induced changes in the absorption coefficient over the spectral region covering both the Ag^+ and Cl^- gap modes are shown in Fig. 6, for E_{dc} along [100] and for the two orthogonal polarization directions. As seen in Fig. 6(a), all of the Ag^+ and Cl^- gap modes shift (slightly) to higher frequencies for $E_{IR} \| E_{dc}$[100]; the shifts are somewhat larger for Ag^+ than for Cl^-. For $E_{IR} \perp E_{dc}$[100] in Fig. 6(b), however, only the Ag^+ pocket gap modes exhibit shifts to lower frequencies comparable in magnitude to those for $E_{IR} \| E_{dc}$[100]; the Cl^- gap modes have no shifts within experimental error. Note that these shifts of the Ag^+ pocket gap modes for $E_{IR} \perp E_{dc}$[100] are unusual: no other previous studies on localized modes have found frequency shifts for this configuration of applied field and polarization,[4,5,19,29,31–33] although we have observed very small shifts in this configuration for the KI:Ag^+ resonant mode, as shown in Fig. 3(a). Figure 6(c) shows the corresponding impurity-induced spectrum at zero applied field for comparison. A very weak line occurs at 75 cm^{-1} in (c) and according to (a) it shifts with field in a direction *opposite* to that of the stronger Ag^+ and Cl^- gap modes. In addition, also seen in (a) [but not in (c)] is a weak field-induced mode at 75.7 cm^{-1}, whose strength grows with the field. The source of the unusual field-induced effects for these weak absorption lines remains unexplained.

A closer look at Fig. 6 reveals that the $E_{IR} \| E_{dc}$[100] frequency shifts of the KI:Cl^- gap modes are more complex than those of the KI:Ag^+ modes: there are actually *four* overlapping Cl^- modes (caused by the natural abundances of Cl^- and K^+ isotopes[34]), each shifting to higher frequency in the parallel polarization by a *different* amount; for the two stronger modes, this is seen more clearly in Fig. 7. Thus, the strongest and highest-frequency mode due to $^{35}Cl^-$ at 77.1 cm^{-1} shifts the least, the weaker middle mode due to $^{37}Cl^-$ at 76.8 cm^{-1} shifts somewhat more, while the extremely weak lowest frequency mode at 76.5 cm^{-1}, which appears only as a shoulder in Fig. 6(c) and is due to a perturbation of the $^{35}Cl^-$ mode by the $^{41}K^+$ isotope,[34] shifts the most. The different sizes of the frequency shifts of the three KI:Cl^- gap modes cause their signatures in the $\Delta\alpha$ plot [Fig. 6(a)] to be similar in size despite the different strengths of the modes involved, particularly in the case of the weak $^{35}Cl^-$:$^{41}K^+$ mode at 76.5 cm^{-1}; however, note that *no* analogous behavior was observed in the uniaxial stress measurements on the Cl^- gap modes.[16] In addition, as seen in Fig. 6(b), whereas the Ag^+ gap modes show substantial perpendicular polarization frequency shifts, *no* such frequency shifts are observed for the Cl^- gap modes, within experimental error. Finally, no frequency shifts were observed for fields along [110] for either the KI:Ag^+ or the KI:Cl^- modes, for *any* polarization, within experimental error. However, the signal-to-noise ratio of the [110] data was somewhat worse than that of the [100] data.

D. Data analysis

The extremely small field-induced frequency shifts of the KI gap modes, presented above, were accurately determined by using the ''global'' analysis method previously developed by us for determining frequency shifts induced by uniaxial

TABLE I. Full widths at half maximum (FWHM's) and strengths of the KI:Ag^+ pocket gap modes under a dc E field in the [100] direction, relative to their zero-field values, at 1.4 K. The 86.2 cm^{-1} mode is the main gap mode, and the 84.5 cm^{-1} mode is caused by the natural abundance of $^{41}K^+$, as discussed in Refs. 8 and 17. The values of the strengths and FWHM's are averages of at least 12 independent measurements; the errors quoted are statistical, not systematic.

Mode (cm^{-1})	Electric field (kV/cm)	Polarization	Rel. FWHM	Rel. strength
86.2	94	$\parallel$	0.999±0.019	0.987±0.026
		$\perp$	0.999±0.003	0.997±0.010
84.5	77	$\parallel$	1.004±0.014	1.007±0.024
		$\perp$	1.002±0.003	1.021±0.024

stress. This method, described in detail in Ref. 16, consists of overlaying the shifted lineshape at some given nonzero field onto the corresponding line shape at zero field and varying the position and width of the nonzero field line shape until the area between the two curves is minimized. The accuracy of the method also allowed us to search for other field-induced line shape changes (such as changes in linewidths or strengths, or the appearance of additional E-field-induced modes): no such effects were detected for the KI:Ag^+ pocket gap modes, as summarized in Table I, i.e., the frequency shifts appear to be ''rigid''.

The frequency shifts of the KI:Ag^+ pocket gap modes obtained for a [100] dc E field are plotted against the square of the magnitude of the field in Fig. 8. The two Ag^+ modes are seen to have very similar E-field behavior: for $E_{IR}\|E_{dc}[100]$ the modes exhibit very small shifts to higher frequency, while for $E_{IR}\perp E_{dc}[100]$ the shifts are to lower frequency. The frequency shifts of the main Ag^+ pocket gap mode at 86.2 cm^{-1} [Fig. 8(a)] are about twice as large for $E_{IR}\|E_{dc}[100]$ than for $E_{IR}\perp E_{dc}[100]$, while the shifts of the Ag^+ isotope pocket gap mode at 84.5 cm^{-1} [Fig. 8(b)] are about the same size in both polarizations. Analogous plots are shown in Fig. 9 for the two relatively strong KI:Cl^- gap modes. By contrast, these two Cl^- modes have significantly *smaller* frequency shifts than the Ag^+ modes for $E_{IR}\|E_{dc}[100]$, and *no* measurable shifts for $E_{IR}\perp E_{dc}[100]$. For $E_{IR}\|E_{dc}[100]$, the shifts of the stronger KI:$^{35}Cl^-$ mode at 77.1 cm^{-1} [Fig. 9(a)] are about half as large as those of the weaker KI:$^{37}Cl^-$ mode at 76.8 cm^{-1} [Fig. 9(b)], in agreement with the discussion of Figs. 6 and 7. Note that the excellent linear fits in the plots of Figs. 8 and 9 indicate that the shifts of both the Ag^+ and Cl^- gap modes are quadratic in the magnitude of the applied field.

As a point of reference, it is useful to note that the *maximum* shift observed for *any* of these gap modes, ~0.02 cm^{-1} at ~100 kV/cm for $E_{IR}\|E_{dc}[100]$ for the main Ag^+ pocket gap mode at 86.2 cm^{-1} [Fig. 8(a)], is much smaller than the full width at half maximum (FWHM) of ~0.5 cm^{-1} of this mode, and is also about two orders of magnitude smaller than the shift of the Ag^+ resonant mode at 17.3 cm^{-1}, which

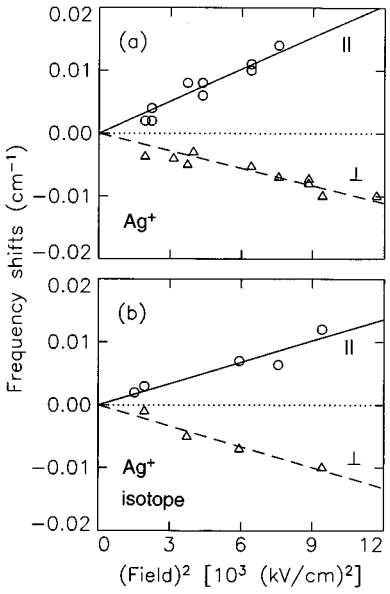

FIG. 8. Frequency shifts of the KI:Ag^+ main and isotope pocket gap modes at 1.4 K vs the square of the magnitude of the [100] E field: (a) the 86.2 cm^{-1} pocket gap mode; (b) the 84.5 cm^{-1} isotope pocket gap mode. The circles (triangles) are the data and the solid (dashed) lines are the best linear fits for $E_{IR}\|E_{dc}$ ($E_{IR}\perp E_{dc}$).

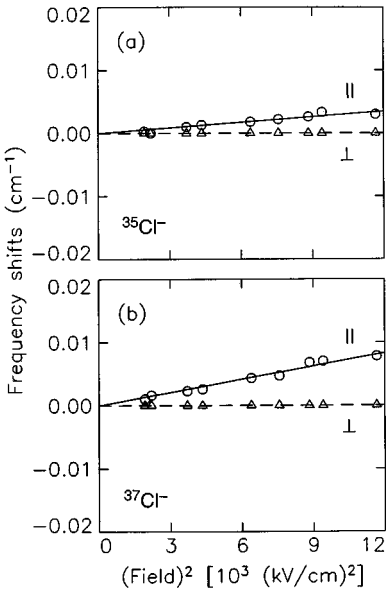

FIG. 9. Frequency shifts of the KI:Cl^- gap modes at 1.4 K vs the square of the magnitude of the [100] E field: (a) the 77.1 cm^{-1} mode; (b) the 76.8 cm^{-1} mode. The circles (triangles) are the data and the solid (dashed) lines are the best linear fits for $E_{IR}\|E_{dc}$ ($E_{IR}\perp E_{dc}$).

has a similar FWHM, at the same value of the applied field;[5] this is clearly seen in Fig. 4 [but note the different resolutions of the spectra in Figs. 4(a) and 4(b)]. The size of the Ag^+ resonant mode shift is comparable to the shifts of resonant modes of other lattice-defect systems;[19,29,31–33] thus, the small sizes of the shifts appear to be a general property of gap modes.

All of the frequency shifts observed to date, for both resonant and gap modes (including those of the Ag^+ gap and resonant modes) are quadratic in the applied field; however, the $E_{IR}\perp E_{dc}[100]$ results for the Ag^+ pocket gap modes are unusual: the typical behavior is a *lack* of any shift in this polarization, as is observed for the Cl^- gap modes and as was previously observed for various resonant modes,[29] including that of Ag^+.[5] Finally, note that the difference between the shifts of the two relatively strong Cl^- gap modes (Fig. 9) is difficult to understand, in that the dynamics of these two modes should be nearly identical (changed only by the mass of the Cl^- ion). Experimentally, one might suspect this difference to be due in part to the weak 76.5 cm^{-1} $^{35}Cl^-$:$^{41}K^+$ mode, mentioned above, which could not be analyzed separately and which appears to shift substantially more than the neighboring and much stronger 76.8 cm^{-1} $^{37}Cl^-$ mode; however, our analysis technique is insensitive to the presence of such a weak mode.

As shown previously,[29] the second-order Stark-effect operator has the same symmetry as the uniaxial stress operator. This implies that the same symmetries of coupling apply to both the quadratic E-field effect and to the uniaxial stress effect. Thus, for an on-center monatomic defect (O_h symmetry), analogs of the $A(A_{1g})$, $B(E_g)$, and $C(T_{2g})$ stress-coupling coefficients discussed in Refs. 3 and 16 can be defined for the quadratic E-field perturbation. The corresponding coefficients in the E-field case are called a_1, a_3, and a_5 in analogy with Ref. 29. As shown in Table II, the equations relating the frequency shifts to the square of the magnitude of the E field are identical to those presented in Table III of Ref. 16 for uniaxial stress, with appropriate substitutions. For the Ag^+ and Cl^- gap modes, the slopes obtained from the measured frequency shifts in Figs. 8 and 9 (for [100] field) are summarized in Table III; these slopes were used to determine the values of the a_1 and a_3 E-field coupling coefficients given in Table IV. For the [110] field direction, the slopes given in Table III are estimated upper bounds obtained from the maximum frequency shifts consistent with the data; the a_5 coupling coefficients calculated from these estimates are also included in Table IV, although their values are not well defined.

TABLE II. Frequency shifts $\Delta\omega$ of the T_{1u} states with the square of the magnitude of the dc E field ΔE^2 along the [100] and [110] crystal directions, for polarization parallel and perpendicular to the applied dc E field (after Ref. 29).

Electric field	Polarization	$\Delta\omega/\Delta E^2$ [10^{-6} cm^{-1}/(kV/cm)^2]
[100]	[100]	a_1+4a_3
[100]	[010]	a_1-2a_3
[110]	[$1\bar{1}0$]	$a_1+a_3+a_5/2$
[110]	[$\bar{1}10$]	$a_1+a_3-a_5/2$

E. Stark effect for other KI gap modes

Since no other E-field measurements on gap modes exist in the literature, we have measured the effect of an applied dc E field on a few other KI gap modes, for the purpose of comparing to the results presented above. However, *no* frequency shifts greater than ± 0.003 cm^{-1} were observed for any other gap mode due to a cation defect (*other than* Ag^+), up to the maximum applied field of $\sim$100 kV/cm in the [100] direction. For example, the Cs^+ and Rb^+ gap modes shown in Fig. 10 have no measurable shifts for either $E_{IR}\|E_{dc}[100]$ [see Fig. 10(a)] or $E_{IR}\perp E_{dc}[100]$ [see Fig. 10(b)], within experimental error; this is in spite of the fact that the KI:Cl^-

TABLE III. Measured slopes ($\Delta\omega/\Delta E^2$) of the frequency shift vs the square of the applied dc E field for various polarizations of the far-IR radiation (E_{IR}) and dc E field (E_{dc}), for the KI:Ag^+ and KI:Cl^- gap modes at 1.4 K, corresponding to Figs. 8 and 9.

Mode	Frequency (cm^{-1})	E_{dc}	E_{IR}	$\Delta\omega/\Delta E^2$ [10^{-6} cm^{-1}/(kV/cm)^2]
KI:Ag^+	86.2	[100]	[100]	1.70±0.09
		[100]	[010]	−0.93±0.05
		[110]	[$1\bar{1}0$]	0.08±0.36
		[110]	[$\bar{1}10$]	0.20±0.29
KI:Ag^+	84.5	[100]	[100]	1.13±0.10
		[100]	[010]	−1.11±0.08
		[110]	[$1\bar{1}0$]	−0.25±0.46
		[110]	[$\bar{1}10$]	0.17±0.20
KI:Cl^-	77.1	[100]	[100]	0.29±0.02
		[100]	[010]	0.00±0.05
		[110]	[$1\bar{1}0$]	0.12±0.12
		[110]	[$\bar{1}10$]	0.08±0.04
KI:Cl^-	76.8	[100]	[100]	0.69±0.02
		[100]	[010]	0.00±0.05
		[110]	[$1\bar{1}0$]	0.24±0.16
		[110]	[$\bar{1}10$]	0.04±0.16

TABLE IV. Measured quadratic E-field coupling coefficients (a_1,a_3,a_5) of the KI:Ag^+ and KI:Cl^- gap modes, calculated from the slopes in Table III, at 1.4 K. The units are 10^{-6} $cm^{-1}/(kV/cm)^2$.

Mode	Frequency (cm^{-1})	a_1	a_3	a_5
KI:Ag^+	86.2	−0.05±0.04	0.44±0.02	−0.12±0.46
	84.5	−0.36±0.06	0.37±0.02	−0.42±0.50
KI:Cl^-	76.8	0.10±0.02	0.05±0.01	0.04±0.13
	77.1	0.23±0.02	0.12±0.01	0.20±0.23

gap modes in the same sample (due to naturally occurring Cl^- impurities), which are similar in strength to the Cs^+ and Rb^+ modes [see Fig. 10(c)], shift noticeably with field for $E_{IR}\|E_{dc}[100]$, as noted in the discussion of Figs. 6 and 7. The estimated uncertainties in the Cs^+ and Rb^+ results are listed in Table V. Analogous results were also obtained for the KI:NCO^- gap mode at 78.4 cm^{-1} (Ref. 35) in a sample whose spectrum is not shown: this mode also had no measurable E-field shifts for either $E_{IR}\|E_{dc}[100]$ or $E_{IR}\perp E_{dc}[100]$ as noted in Table V.

In contrast, the isotopically split KI:Br^- gap mode doublet at 88.1 and 88.65 cm^{-1} (Ref. 36) displayed a very small and qualitatively different effect, as shown in Fig. 11(a): for $E_{IR}\|E_{dc}[100]$, the lower-frequency mode appears to shift down and the upper-frequency mode appears to shift up with increasing field. This leads to an unusual signature in the difference spectrum, where the derivative-like line shapes of the two members of the Br^- doublet have opposite signs, unlike the case of the Cl^- doublet, whose derivative-like line shapes have the same signs. The different signatures of these doublets in Fig. 11(a) can best be appreciated by reference to the zero-field spectrum of Fig. 11(c), where the Br^- and Cl^- doublets are seen to be similar. The shift of the Br^- mode at 88.1 cm^{-1} to lower frequency with increasing field is highly unusual: all other modes studied to date, including all other KI gap modes studied in this work, shift to higher frequency with increasing field. Smaller effects are observed for the Br^- doublet for $E_{IR}\perp E_{dc}[100]$, as seen in Fig. 11(b). In addition, as shown in Fig. 11(a) and (b) *no* measurable E-field-induced shift is observed for either polarization for the relatively strong KI:Br^- pair mode at 74 cm^{-1} seen in Fig. 11(c).

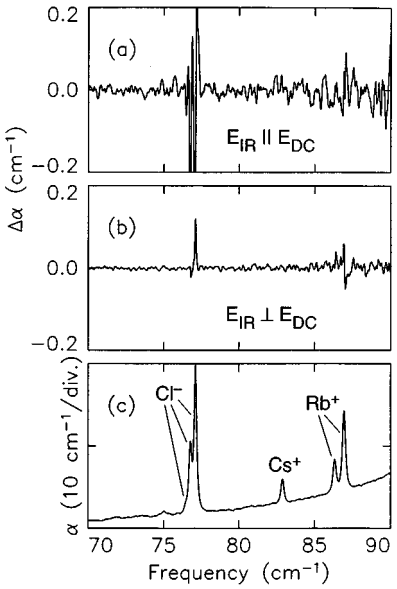

FIG. 10. Changes in the absorption coefficient of KI+0.02 mole % CsI+0.02 mole % RbI induced by a [100] E field of 85 kV/cm. The resolution is 0.1 cm^{-1} and the temperature is 1.4 K. (a) $E_{IR}\|E_{dc}$. (b) $E_{IR}\perp E_{dc}$. (c) The corresponding spectrum at zero applied field. Note that *no* frequency shifts are observed for the KI:Rb^+ gap mode doublet (at 86.3 and 86.9 cm^{-1}) and for the Cs^+ gap mode (at 82.9 cm^{-1}). The Cl^- gap modes at 76.8 and 77.1 cm^{-1} are nearly saturated in this sample, as is the 86.9 cm^{-1} Rb^+ mode.

The unusual shifts for the KI:Br^- doublet at 88.1 and 88.65 cm^{-1} for $E_{IR}\|E_{dc}[100]$ are shown on an expanded scale in Fig. 12. In addition to the opposite signs of the shifts of the two modes mentioned above, this figure also reveals a possible transfer of absorption strength from the higher- to the lower-frequency member of the doublet. This is again qualitatively different from the case of the KI:Cl^- gap modes discussed above, which shift *rigidly* to higher frequencies with increasing field (albeit at different rates; see Fig. 9).

Several other peculiar characteristics of the KI:Br^- sample deserve mention: First, the absorption strength per impurity for Br^- in KI is lower than that for any other impurity measured [cf. the Cs^+ and Rb^+ gap modes in Fig. 10(c), and note the order-of-magnitude difference between the impurity concentration of the sample used for the spectrum of Fig. 10(c) and that used for Fig. 11(c)]. This comparison also applies to Ag^+ [see Fig. 6(c)], although the effective Ag^+ concentration is more difficult to define due to

TABLE V. Frequency shifts of the KI:Cs^+, KI:Rb^+, and KI:NCO^- gap modes under an applied dc E field in the [100] direction at 1.4 K. The values are given relative to the zero-field values and represent averages of at least six independent measurements; the errors quoted are statistical, not systematic.

Mode	Frequency (cm^{-1})	Field (kV/cm)	Polarization (∥ or ⊥)	Shift (cm^{-1})
Cs^+	82.9	85	∥	0.000±0.003
			⊥	0.000±0.001
Rb^+	86.3	85	∥	0.001±0.003
			⊥	0.001±0.002
Rb^+	86.9	85	∥	0.000±0.002
			⊥	−0.001±0.002
NCO^-	78.4	97	∥	0.000±0.001
			⊥	0.000±0.001

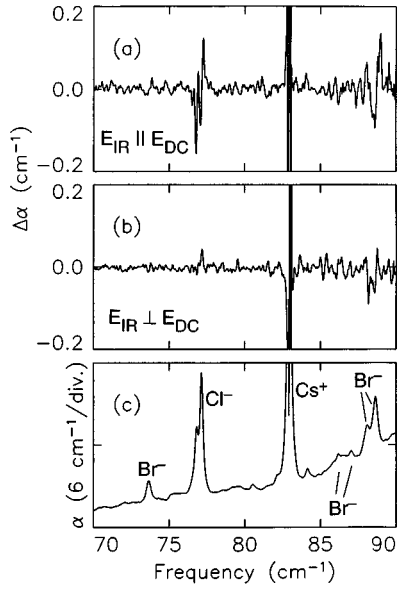

FIG. 11. Changes in the absorption coefficient of KI+0.15 mole % KBr+0.02 mole % CsI induced by a [100] E field of 85 kV/cm. The resolution is 0.1 cm^{-1} and the temperature is 1.4 K. (a) $E_{IR} \| E_{dc}$. (b) $E_{IR} \perp E_{dc}$. (c) The corresponding spectrum at zero applied field. Note that very small frequency shifts are observed for the KI:Br^- gap mode doublet (at 88.1 and 88.65 cm^{-1}) but not for the Br^- pair mode at 74 cm^{-1}. Other weak modes seen here, identified previously as being due to Br^- (Ref. 36), show no measurable shift with field. The KI:Cs^+ gap mode at 82.9 cm^{-1} is saturated in this sample.

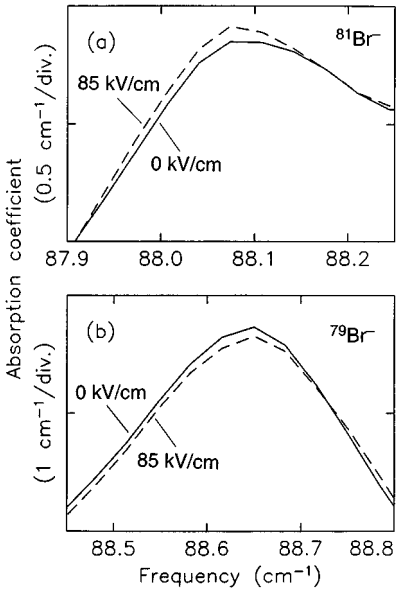

FIG. 12. Spectra of the relatively strong isotopically split KI:Br^- gap mode doublet with *no* applied E field (solid lines) and with an applied [100] E field (dashed lines) of 85 kV/cm for $E_{IR} \| E_{dc}$. The resolution is 0.1 cm^{-1} and the temperature is 1.4 K; the sample is the same as in Fig. 11. (a) The 88.1 cm^{-1} $^{81}Br^-$ gap mode. (b) The 88.65 cm^{-1} $^{79}Br^-$ gap mode. Note that the ordinate scale in (a) is expanded 2× relative to that in (b).

its peculiar ''aging'' effect.[28] Second, the high concentrations required to observe the Br^- gap modes lead to relatively large changes in the average lattice constant of the KI host and hence to shifts in the frequencies of the impurity modes and broadening of the line shapes: thus, the frequencies of the Br^- modes reported here are ~0.4 cm^{-1} lower than those in Ref. 36 and the frequencies of the Cl^- modes, due to the naturally occurring Cl^- impurities in this sample, are ~0.05 cm^{-1} higher than measured in a crystal with much lower impurity concentrations; the Cl^- modes are also broadened in this sample (compare Fig. 11 to Fig. 6). The shift in the frequencies of the Cl^- modes are in good agreement with Vegard's law,[19] which predicts a shift of 0.03 cm^{-1} using the Cl^- A_{1g} stress coupling coefficient measured previously[16] and a nominal Br^- concentration of 0.15 mole %. Finally, although Fig. 11 shows that the shifts of the two relatively strong Cl^- gap modes in this sample are approximately the same size as in an unstrained sample (cf. Fig. 6), no evidence is observed of the unusually large shift of the weak KI:Cl^- mode at 76.5 cm^{-1}: noted in Fig. 6: the strain induced by the high Br^- concentration in this sample appears to perturb the ''asymmetrical'' $^{35}Cl^-$:$^{41}K^+$ gap mode[34] much more strongly than either of the ''symmetrical'' $^{35}Cl^-$ and $^{37}Cl^-$ gap modes.

An attempt was also made to investigate the E-field effect on the strong KI:F-center gap mode at 82.7 cm^{-1}.[37] An excimer laser was used to create the F centers in a KI crystal at room temperature prior to the measurement, as described previously,[16] and the far-IR spectra following irradiation showed an F-center gap mode comparable in strength to the other KI gap modes discussed above. However, it was found that the irradiated samples could not sustain even a field of <40 kV/cm for more than a few minutes: apparently, the F centers are still somewhat mobile under an applied E field even at liquid-He temperatures.

III. THEORY

In our original harmonic perturbed shell model for the KI:Ag^+ on-center configuration dynamics,[7] the defect is characterized by its mass and by assumed defect/nearest neighbor $(0-1n)$ longitudinal force-constant changes, $\delta_1 = -\Delta\Phi_{xx}(000,100)$, and relaxation-induced nearest-neighbor/fourth-nearest neighbor $(1n-4n)$ longitudinal force-constant changes, $\delta_2 = -\Delta\Phi_{xx}(100,200)$. All of the other short- and long-range force constants are assumed to remain unperturbed by the defect. We will refer to this as the (δ_1,δ_2) model, which is discussed extensively in Ref. 8. The force-constant changes (δ_1,δ_2) are fit to the measured T_{1u} resonant and gap mode frequencies of 17.3 and 86.2 cm^{-1}, respectively, yielding the values given in the first row of Table VI. The model then predicts an E_g resonant mode at 20.5 cm^{-1}, in fair agreement with the measured Raman peak at 16.1 cm^{-1}.[5,7] In addition, as discussed in the introduction, the model also predicts nearly degenerate pocket gap modes of different symmetries: an A_{1g} (nondegenerate) mode at 87.2 cm^{-1}, an E_g (twofold degenerate) mode at 86.0 cm^{-1}, and the T_{1u} (threefold degenerate) mode at 86.2 cm^{-1}. The displacement patterns of these modes are peaked strongly *away* from the defect, on the family of six (200) sites.[8]

In Ref. 16 we combined this harmonic model with a simple model for the anharmonicity in order to fit nearest-neighbor cubic anharmonicities near the (200) sites to mea-

TABLE VI. Theoretical KI:Ag^+ resonant and gap mode frequencies, and the force-constant changes (δ_1,δ_2) for the three harmonic defect models considered in the text, compared with experiment. The (δ_1,δ_2) model is the model used in Refs. 1, 7, 8, and 17. The $(\delta_1,\delta_2,\delta_3)$ model adds a relaxation-induced force-constant change, $\delta_3=0.6\delta_2$, to the (δ_1,δ_2) model; this is done without adding any free parameters to the (δ_1,δ_2) model, as discussed in the text. The QD model adds both the relaxation-induced force-constant change, $\delta_3=0.6\delta_2$, and a Ag^+ electronic quadrupolar deformability force-constant change to the (δ_1,δ_2) model. For all three models, δ_1 and δ_2 are fit to the experimental T_{1u} resonant and gap mode frequencies. The additional quadrupolar force constant change present in the QD model is fit to the experimental E_g resonant mode frequency. The force-constant changes are given as fractions of the KI nearest-neighbor longitudinal overlap (shell-shell) force constant, $k=18.84$ N/m, of the breathing shell model. All frequencies are given in cm^{-1}.

Model	δ_1/k	δ_2/k	T_{1u}	T_{1u}	E_g	A_{1g}
(δ_1,δ_2)[a]	−0.563	−0.531	17.3 (fit)	86.2 (fit)	20.5	37.3
$(\delta_1,\delta_2,\delta_3)$	−0.585	−0.291	17.3 (fit)	86.2 (fit)	26.3	41.5
QD	−0.585	−0.291	17.3 (fit)	86.2 (fit)	16.1 (fit)	41.5
Experiment[b]			17.3	86.2	16.1	[c]

[a]See Ref. 8.
[b]See Ref. 7.
[c]Not observed (see Ref. 7).

sured stress-induced frequency shifts of the T_{1u} IR-active pocket gap mode. The resulting stress-fit anharmonicities were unusual, in that they predicted that a stress-induced decrease in the (100)-(200) ion separation would cause the (100)-(200) longitudinal force constant to *weaken*, in sharp contrast to the force-constant strengthening expected for the usual repulsive-dominated model potentials which describe typical alkali-halide nearest-neighbor interactions.[38] However, the standard alkali-halide potential anharmonicities are unable to reproduce the measured anomalous E_g symmetry stress coupling, which is responsible for our unusual stress-fit anharmonicities in the first place.[16]

The stress-fit anharmonicities amount to a reparametrization of the pocket-mode stress measurements. In order to check these anharmonicities, we have developed a theory for the dc E-field-induced frequency shifts analogous to our stress theory, and we combine it with our stress-fit anharmonicities to predict the pocket-gap-mode static E-field-induced frequency shifts. These are then compared to the measured shifts discussed earlier. In our theory, the dc E-field-induced force-constant changes linear in the applied field are determined from the predicted E-field-induced microscopic ''strains'' via cubic anharmonicities. These force constant changes are then combined with computed pocket-gap-mode normalized displacement patterns to calculate the predicted field-induced frequency shifts. This procedure for calculating the field-induced pocket-gap-mode shifts is outlined in Fig. 13 and is described in greater detail in the Appendix.

The local ''strains'' needed are the E-field-induced ionic displacements near the defect. As was the case for the local stress-induced ionic displacements discussed in Ref. 16, these field-induced displacements will be strongly affected by the force-constant changes (δ_1,δ_2) in our model. For the case where the applied forces in the pure and defect crystals are identical, Elliot, Krumhansl, and Merrett[39] have shown how to relate the local microscopic defect-crystal strains to their pure-crystal counterparts, using zero-frequency perturbed harmonic Green's functions. As long as we assume that the effective charges coupling the field to the ions remain unchanged by the introduction of the defect, this method applies to the E-field-induced strains as well as to the stress-induced strains. As a result, the pure-crystal E-field-induced ionic displacements can be readily converted to local displacements near the defect.

For a dc field applied along the $\hat{x}$ direction, we find that the resulting displacements are strongly dominated by those on the Ag^+ impurity and its two nearest-neighbor I^- ions at

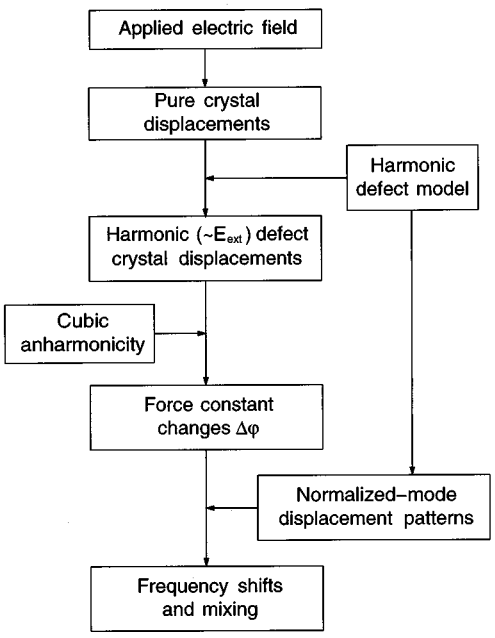

FIG. 13. Schematic diagram illustrating the procedure for calculating the static E-field-induced mixing for both the KI:Ag^+ pocket gap modes and low-frequency resonant modes. Note that the defect-crystal E-field-induced displacements and the normalized mode-displacement patterns are both determined from the harmonic defect theory. The anharmonicity is only needed to determine the force-constant changes produced by the local E-field-induced displacements in the defect crystal.

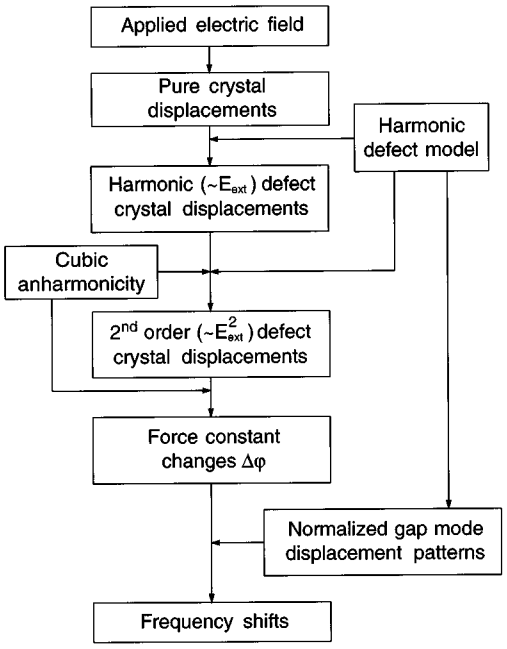

FIG. 14. Schematic diagram illustrating the procedure for calculating the static E-field-induced cubic-cubic $E_{\rm dc}^2$ frequency shifts for the KI:Ag^+ gap modes. Note that the anharmonicity is needed to determine both the second-order E-field-induced displacements and the force-constant changes produced by these displacements.

(± 100). This is consistent with the large force-constant weakening at the defect and nearest-neighbor sites in our (δ_1,δ_2) model.

The first-order defect-crystal E-field-induced ionic displacements, when combined with cubic anharmonicity, produce harmonic force-constant changes linear in the applied field. These force-constant changes would not affect an isolated T_{1u} mode. However, they can *mix* the nearly degenerate A_{1g}, E_g, and T_{1u} pocket gap modes, producing frequency shifts and IR activity for modes of all three symmetries. We treat these force-constant changes as small and perform a nearly degenerate perturbation-theory calculation in order to determine this mixing. Although these force-constant changes are linear in the applied field, it turns out that for our QD model, which will be discussed later, the predicted mixing is sufficiently small that force-constant changes produced by *second*-order ($\sim E_{\rm dc}^2$) E-field-induced strains generate frequency shifts which are comparable to shifts predicted by the mixing. Our procedure for calculating the force-constant changes produced by these higher-order strains is outlined in Fig. 14 and is described in more detail in the Appendix. In essence, we use the stress-fit cubic anharmonicities, coupled with calculated first-order defect-crystal E-field-induced strains, to determine quadratic ($\sim E_{\rm dc}^2$) cubic-anharmonicity corrections to the first-order strains. We then compute the lowest-order force-constant changes produced by these $E_{\rm dc}^2$ strains. Notice that the cubic anharmonicity is used twice here: once to calculate the second-order strains, and again to determine the force-constant changes produced by these strains. Hence, we will refer to the E-field-induced force-constant changes and the resulting mode coupling produced by these second-order displacements as ''cubic-cubic'' force-constant changes and mode coupling.

In addition to the cubic-cubic mechanism, the first-order field-induced displacements, when coupled to *quartic* anharmonicity, also produce force-constant changes quadratic in $E_{\rm dc}$. Moreover, the coupling produced by these force-constant changes has the same symmetry properties as the cubic-cubic coupling. Hence, these two second-order effects cannot be separated on the basis of symmetry arguments. Unfortunately, the stress calculation only determines *cubic* anharmonicities. We will estimate the shifts produced by the quartic anharmonic mechanism using Born-Mayer anharmonicities whenever these second-order effects cannot be neglected.

A. (δ_1,δ_2) model pocket-mode shifts and mixing

We will now apply the quasiharmonic theory outlined above to our (δ_1,δ_2) model and predict the E-field-induced frequency shifts and mixing for the KI:Ag^+ pocket gap modes using the nearest-neighbor stress-fit cubic anharmonicities determined in Ref. 16. In that work, we assumed that the dominant stress-induced force-constant changes arise from the strong and rapidly varying short-range overlap forces and, as a result, we restricted our attention to nearest-neighbor cubic anharmonicities. Furthermore, we assumed that these anharmonicities are derivable from central potentials, and we make the same assumptions here. Since the pocket modes are strongly peaked on the fourth-neighbor sites, (± 200), (0 ± 20), and (00 ± 2), we will first identify the cubic anharmonic coefficients needed to calculate the E-field-induced force-constant changes between the (200) site and its nearest neighbors. As we will show, the set of anharmonic coefficients needed to determine these force-constant changes includes the anharmonic coefficients necessary to determine the E-field-induced force-constant changes between all of the nearest-neighbor pairs of ions used in the pocket-mode field-induced frequency shifts calculation. Hence, the anharmonicities between the (200) site and its nearest neighbors are the only independent anharmonicities we need to consider for our (δ_1,δ_2) model.

In our pocket-mode stress study,[16] we reduced to three the number of independent anharmonic coefficients needed to determine the pocket-mode stress-induced frequency shifts by using various symmetry and model consistency arguments and, for clarity, we now summarize those arguments. Symmetry considerations, together with the central potential assumption, reduce to nine the number of independent cubic anharmonic coefficients needed to determine the force-constant changes between the (200) site and its nearest neighbors. Only six of these nine coefficients are needed to determine the stress and E-field induced frequency shifts:

$$A_1 \equiv \Phi_{xxx}(100,100,200), \quad A_2 \equiv \Phi_{xxx}(200,200,300),$$

$$B_1 \equiv \Phi_{yxy}(100,100,200), \quad B_2 \equiv \Phi_{xxz}(200,200,201),$$

$$B_3 \equiv \Phi_{yxy}(200,200,300), \quad C_2 \equiv \Phi_{xxx}(200,200,201).$$

These coefficients are appropriate to the zero-field, unstressed defect-crystal equilibrium configuration, of course. Since in our (δ_1,δ_2) model only the (000)-(100) and (100)-(200) longitudinal force-constant changes are perturbed, we will treat A_2, B_2, B_3, and C_2 as pure crystal coefficients, as

we did in the stress paper.[16] This leads to $C_2 \equiv 0$ and $B_3 \equiv B_2$. Moreover, B_2 involves just $V'(r)$ and $V''(r)$, both of which may be obtained from the known nearest-neighbor overlap (shell-shell) force constants of the breathing shell model,[40] together with the Coulomb interaction. Knowing B_2, this leaves us with three unknown independent anharmonic parameters, namely A_1, A_2, and B_1, which were fit to the three measured stress-induced coupling coefficients.[16] Note that since A_2 and B_2 are coefficients appropriate to the pure crystal, we have at the same time determined the anharmonic coefficients necessary to calculate the E-field-induced force-constant changes between any two adjacent host ions, other than the (100)-(200) family involved in our (δ_1,δ_2) model. Since the pocket modes have such small displacements on the defect and the defect's nearest neighbors, these are the only anharmonicities we need in addition to the anharmonicities between the (200) site and its nearest neighbors, in order to calculate the field-induced pocket-gap-mode shifts.

As was the case with the stress calculation,[16] we found it necessary to include contributions from other sites besides the fourth neighbors in our static E-field calculations of the gap-mode mixing. In particular, for the (δ_1,δ_2) model, we included contributions from the (100), (200), (300), (400), (500), (600), (101), (201), and (301) sites, together with sites equivalent to these by symmetry. Calculations including additional displacements produce changes of less than 1% in the predicted E-field-induced gap-mode coupling coefficients. This small change in the coupling is negligible compared to the larger uncertainties ($\sim$13%) in our stress-fit cubic anharmonicities, and we will thus neglect these additional displacements in our calculations. Furthermore, similar arguments show that we do not need to consider additional displacements beyond those listed above in order to determine the E-field-induced mode coupling for any of the other models considered in this paper.

As shown in the Appendix, a dc E-field applied along the [100] direction mixes the E_g2, $T_{1u}x$, and A_{1g} pocket modes. Here $T_{1u}x$ denotes the T_{1u} partner which couples to x-polarized radiation, and E_g2 denotes one of the two degenerate E_g partners. For the strongest [100] applied field in our experiments, namely 87 kV/cm, we predict three mixed modes, at frequencies 84.5, 86.8, and 88.2 cm^{-1}; as the field is reduced to zero, these become the unperturbed E_g, T_{1u}, and A_{1g} pocket modes at 86.0, 86.2 and 87.2 cm^{-1}, respectively. The absorption strengths of these mixed modes for 87 kV/cm are, relative to that of the zero-field T_{1u} pocket gap mode, S_x=0.38, 0.11, and 0.51, respectively. Thus the original IR-active T_{1u} pocket mode loses most of its absorption strength, while the original even-parity A_{1g} and E_g pocket modes acquire substantial T_{1u} character and consequent IR activity.

The measured parallel polarization shift in peak position of the T_{1u} pocket gap mode at 1.4 K is shown by the solid curve in Fig. 15(a) for the same applied field considered above. The other panels of Fig. 15 compare the experimental difference spectra with the predictions of our $(\delta_1,\delta_2,\delta_3)$ and QD models, which will be discussed in Secs. III B and III C, respectively. The measured spectrum shown in this figure was created by subtracting the IR-absorption spectrum measured with the field off from the spectrum measured with the field on. To compare this result to our model predictions in

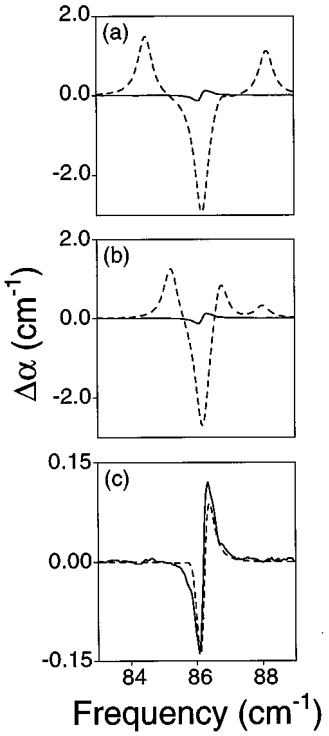

FIG. 15. Experimental Stark-effect difference spectra for the Ag^+ pocket modes, compared with the predictions of the three models. The measured spectrum, $\Delta\alpha \equiv \alpha(E_{dc}=87$ kV/cm$) - \alpha(E_{dc}=0$ kV/cm) for $E_{IR} \| E_{dc}[100]$, is given by the solid curves. The theoretical predictions are given by the dashed curves: (a) (δ_1,δ_2) model, (b) $(\delta_1,\delta_2,\delta_3)$ model, and (c) QD model. Both the (δ_1,δ_2) and $(\delta_1,\delta_2,\delta_3)$ model predictions are an order of magnitude too large. In order to generate the predicted difference spectra, we assigned a Voigt line shape to each mode predicted by our mixing calculation, as discussed in the text. (Note that the QD model calculated frequency shifts of Table X are given directly by the theory, with no line-shape assumptions needed.)

Fig. 15, we assigned a Voigt line shape to each of the mixed modes and subtracted this spectrum from our predicted zero-field spectrum. The Voigt line shape was determined from the measured zero-field line shape for the IR-active T_{1u} pocket gap mode.[8,17] For the nonzero field case, we also used this line shape, but at our predicted frequency and with a strength obtained by combining the observed zero-field strength with our predicted *relative* strength for each IR-active pocket mode. This procedure was followed for each of the three model calculations shown in Fig. 15. For our (δ_1,δ_2) model of Fig. 15(a), the mixing is large and, hence, second-order effects, such as the cubic-cubic coupling, were neglected in our calculation of the predicted difference spectrum. Notice that the predicted (δ_1,δ_2) model difference spectrum differs dramatically from the measured spectrum. The measured difference spectrum corresponds to an E-field-induced frequency shift of $\sim$0.015 cm^{-1}, which is small compared to the unperturbed mode linewidth (FWHM) of $\sim$0.5 cm^{-1}. In sharp contrast, our (δ_1,δ_2) model predicts frequency shifts nearly two orders of magnitude larger. Carrying through the stress-fit anharmonicity uncertainties in the calculation does not significantly improve the agreement between theory and experiment. In addition, note that the shape

of the measured difference spectrum closely resembles the derivative of the unperturbed line shape, which is what one would expect when the mode is shifted rigidly in frequency by the field with no mixing. In contrast, the three-peak difference spectrum predicted by our (δ_1,δ_2) model reflects the strong mixing in this model, where both of the even-parity pocket modes acquire significant T_{1u} character and IR activity.

If we use cubic anharmonicities calculated from Coulomb plus Born-Mayer potentials consistently fit to our model's defect-induced harmonic force constant changes and breathing shell model parameters (see Ref. 16), the predicted E-field-induced mixing turns out to be over an order of magnitude smaller than that predicted using the stress-fit anharmonicities. In Ref. 16, we were able to obtain Born-Mayer-like nearest-neighbor stress-fit anharmonicities (i.e., anharmonicities consistent with a repulsive-dominated potential) using our (δ_1,δ_2) model by weakening our δ_2 force-constant change beyond its fit value to the measured IR spectra. However, we were not able to find a δ_2 force constant weak enough to do this and also maintain a reasonable fit to the measured IR spectra. This suggests that in order to reconcile our theory for the on-center dynamics of KI:Ag^+ with the measured pocket-gap-mode stress and E-field results, we should attempt to reproduce these Born-Mayer-like stress-fit anharmonicities and maintain our agreement with the IR spectra by adding other harmonic force-constant changes to our original (δ_1,δ_2) model. The question is whether we can do this without introducing an unreasonable number of new parameters and without destroying the successful results of Refs. 8 and 17 and for the pocket-mode isotope effect.

B. $(\delta_1,\delta_2,\delta_3)$ model pocket-mode shifts and mixing

Our (δ_1,δ_2) model assumes that defect-induced inward static relaxation of the silver ion's six nearest neighbors relative to their pure crystal positions produces the force-constant change $\delta_2=-\Delta\Phi_{xx}(100,200)$. The magnitude of its fit value is roughly half the pure KI nearest-neighbor overlap force constant (see Table VI). This large value implies that the (100)-(200) relaxation is substantial, suggesting that (200)-(300) relaxation-induced force-constant changes could also be important. Moreover, a $\delta_3\equiv-\Delta\Phi_{xx}(200,300)$ force-constant change would have a strong effect on the pocket-gap-mode frequencies since the displacement patterns for these modes are peaked on the fourth-neighbor sites, (200). Page[20] has shown that this force-constant change (and its analogs $\delta_n\equiv-\Delta\Phi_{xx}[(n-1)00,n00]$) can be determined without introducing *any* new parameters, as follows. If we make the reasonable assumption that the presence of an isoelectronic defect, such as Ag^+, in the *unrelaxed* crystal produces radial forces on just the defect's six nearest neighbors and work within a linearized theory (i.e., small relaxations), we can use the pure crystal harmonic shell model static Green's functions to compute the static displacements throughout the lattice, *relative* to those on the defect's six nearest neighbors. These "relative" static relaxations are largest along the six (100) directions. If we combine these relative relaxations with the assumption of cubic anharmonicity arising from central potentials between adjacent host lattice ions, we can then compute the force-constant change δ_3 *uniquely* in terms of δ_2. For KI this procedure yields $\delta_3=0.6\delta_2$.[20] This result has been obtained without adding any free parameters to the (δ_1,δ_2) model.

TABLE VII. Predicted harmonic properties for the three defect models discussed in the text, compared with experiment. First column: frequency shifts of the T_{1u} resonant mode for a defect isotope substitution ($^{107}Ag^+\rightarrow{}^{109}Ag^+$). Second column: shifts of the T_{1u} pocket gap mode for a host isotope substitution ($^{39}K^+\rightarrow{}^{41}K^+$). Third column: ratio of the absorption strength of the isotope pocket gap mode to that of the unperturbed 86.2 cm^{-1} pocket gap mode for a 7% natural abundance of $^{41}K^+$. Fourth column: the absorption strength ratio for the T_{1u} gap and resonant modes. None of the parameters of these models were adjusted to fit the measurements.

Model	$\Delta\omega$ (cm^{-1}) res. mode	$\Delta\omega$ (cm^{-1}) gap mode	S_i/S_g	S_g/S_r
(δ_1,δ_2)	−0.05	−1.46	0.073	1.4
$(\delta_1,\delta_2,\delta_3)$	−0.12	−1.63	0.074	3.0
QD	−0.12	−1.64	0.073	3.0
Expt.	-0.14 ± 0.03[a]	−1.7	0.04	3[b]

[a]Reference 2.
[b]Reference 7.

For this new "relaxation model" $(\delta_1,\ \delta_2,\delta_3)$, we again fit δ_1 and δ_2 to the measured IR T_{1u} resonant and gap mode frequencies. Table VI summarizes the results of these fits. As before, we find three nearly degenerate A_{1g}, E_g, and T_{1u} pocket gap modes with displacements strongly peaked on the defect's fourth-neighbor sites. The predicted E_g and A_{1g} gap-mode frequencies are 86.0 and 87.8 cm^{-1}, respectively, which are almost identical to the frequencies predicted by the (δ_1,δ_2) model. The second row of Table VII lists other predicted harmonic properties for the $(\delta_1,\delta_2,\delta_3)$ model, and all are seen to be in substantially better agreement with experiment than for the (δ_1,δ_2) model, except the predicted pocket gap mode isotope strength, which remains essentially unchanged. Despite the improvements shown in Table VII and the fact that the $(\delta_1,\delta_2,\delta_3)$ model is well motivated physically, this model has at least one serious drawback: it predicts a Raman-active E_g symmetry resonant mode at 26.3 cm^{-1}, 10 cm^{-1} above the measured frequency and 6 cm^{-1} above the (δ_1,δ_2) model prediction, as indicated in Table VI.

We now turn to the anharmonic predictions of this model. In the $(\delta_1,\delta_2,\delta_3)$ model, the (200)-(300) longitudinal force constant is perturbed in addition to the (000)-(100) and (100)-(200) longitudinal force constants. In Sec. III A, we used the fact that the (δ_1,δ_2) model only perturbs the (000)-(100) and (100)-(200) force constants in order to justify treating just the $A_1=\Phi_{xxx}(100,100,200)$ and $B_1=\Phi_{yxy}(100,100,200)$ cubic anharmonic coefficients as defect-crystal coefficients, and all others as pure crystal coefficients. For consistency, we now need to treat $A_2=\Phi_{xxx}(200,200,300)$ and $B_3=\Phi_{yxy}(200,200,300)$, in addition to A_1 and B_1, as defect-crystal anharmonicities. This introduces two new free anharmonic parameters into our quasiharmonic theory. However, we can use the same defect-induced relative relaxations argument outlined above and used for computing the harmonic force constant δ_3 in terms of δ_2, to show that $(A_2-A_3)=0.6(A_1-A_3)$ and $(B_4-B_3)=0.6(B_4-B_1)$, where we have introduced the *pure*-crystal anharmonic coefficients $A_3=\Phi_{xxx}(300,300,400)$

TABLE VIII. Anharmonic parameters determined from the KI:Ag^+ T_{1u} gap mode stress coupling coefficients, A, B, and C, measured in Ref. 16, for the three harmonic defect models discussed in the text. For comparison, the last row gives the anharmonicities obtained by fitting a Coulomb plus Born-Mayer potential to the harmonic parameters of the QD model. The units are 10^{12} dyn/cm^2.

Model	A_1	A_2	B_1
(δ_1,δ_2)[a]	6±1	−17±3	3±4
$(\delta_1,\delta_2,\delta_3)$	9±2	−7±1	2.3±2.7
QD	−0.56±0.37	−4.2±0.5	2.3±2.7
BM-QD	−4.18	−5.11	0.004 03

[a]Reference 16.

and $B_4=\Phi_{yxy}(300,300,400)$. In order to derive these relations, we have assumed that the dominant relaxation-induced change in these cubic anharmonicities is produced by pure-crystal quartic anharmonicity arising from nearest-neighbor central potentials. Furthermore, we have assumed that A_3 and B_4 are pure crystal anharmonicities since the (300)-(400) harmonic force constants are not perturbed in the $(\delta_1,\delta_2,\delta_3)$ model. Furthermore, point symmetry and the central potential assumption lead to $B_4=B_2=\Phi_{xxz}(200,200,201)=2.0193\times10^{11}$ dyn/cm^2. Using these approximations, we have again reduced to three the number of free anharmonic parameters, which can then be fit to the three measured pocket-gap-mode stress coefficients, exactly as for the (δ_1,δ_2) model.

The resulting stress-fit anharmonicities for the $(\delta_1,\delta_2,\delta_3)$ model are listed in Table VIII, and the corresponding E-field-induced difference spectrum predicted using these fit anharmonicities is given in Fig. 15(b). Notice that the $(\delta_1,\delta_2,\delta_3)$ model stress-fit anharmonicities given in Table VIII are similar to our earlier (δ_1,δ_2) model anharmonicities, and hence they suffer from the same shortcomings. More importantly, notice that the $(\delta_1,\delta_2,\delta_3)$ model prediction for the E-field-induced difference spectrum shows little or no improvement over the (δ_1,δ_2) model spectrum—the predicted field-induced frequency shifts for the $(\delta_1,\delta_2,\delta_3)$ model also exceed the measured shifts by nearly two orders of magnitude.

C. QD model pocket-mode shifts and mixing

A consistent explanation of the measured stress and E-field pocket-gap-mode shifts is obtained by adding to the $(\delta_1,\delta_2,\delta_3)$ model a Ag^+ quadrupolar deformability (QD) induced harmonic force-constant change, $\delta_{QD}\equiv\Delta\Phi_{xx}(100,-100)=2\Delta\Phi_{xy}(100,010)$, together with symmetry-related terms reflecting the O_h symmetry of the defect, such as $\Delta\Phi_{yy}(010,0-10)=2\Delta\Phi_{xz}(100,001)=\delta_{QD}$. Quantum mechanically, such force-constant changes arise from virtual s-d electronic transitions and have been argued to be important for the Ag^+ ion.[21–27,41] This force-constant change couples exclusively to E_g symmetry modes, and thus we expect it to have a strong effect upon the E_g symmetry resonant-mode frequency and stress-induced displacements, which are the quantities we want to change.

Our QD model adds but a *single* free harmonic parameter to those included in the original (δ_1,δ_2) model; δ_3 is still determined uniquely in terms of δ_2, as described above. As before, we obtain the force-constant changes δ_1 and δ_2 by fitting the measured IR resonant and pocket-gap-mode peaks at 17.3 and 86.2 cm^{-1}, and hence we necessarily obtain the previous $(\delta_1,\delta_2,\delta_3)$ model values since δ_{QD} does not affect T_{1u} symmetry modes. Having fit two of the three harmonic model parameters, we then adjust δ_{QD} to reproduce the measured 16.1 cm^{-1} E_g Raman peak. The results of these fits are summarized in Table VI. The QD model still predicts three nearly degenerate A_{1g}, E_g, and T_{1u} pocket gap modes, which are virtually identical in frequencies and displacement patterns to the pocket gap modes predicted by the (δ_1,δ_2) and $(\delta_1,\delta_2,\delta_3)$ models. Moreover, the resulting predicted harmonic properties of Table VII (third row) are seen to retain the markedly improved agreement with experiment of the $(\delta_1,\delta_2,\delta_3)$ model. Hence, by the addition of the single δ_{QD} force-constant change parameter, we have been able to correct the only serious drawback of the harmonic predictions of the $(\delta_1,\delta_2,\delta_3)$ model, namely its predicted E_g resonant mode frequency, without losing the $(\delta_1,\delta_2,\delta_3)$ model's improved agreement with other experimental harmonic results.

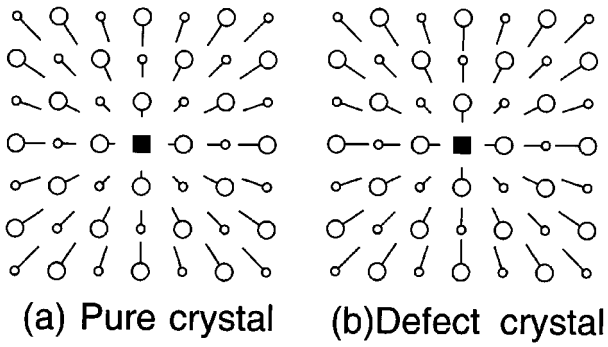

FIG. 16. Calculated KI:Ag^+ stress-induced A_{1g} symmetry displacements in the x-y plane for (a) the pure crystal and (b) the QD model. The pure-crystal and defect-crystal strains are plotted to the same scale. The displacements are linear in the applied stress, and the scale was chosen to show the displacement pattern clearly. Since none of the calculations of this paper require knowledge of the absolute equilibrium positions of the ions in the unstressed, zero E-field, defect lattice, the stress-induced displacements shown here and in Fig. 17 are drawn with respect to the pure host-crystal equilibrium positions.

The QD model values for the stress-fit anharmonicities are listed in the third row of Table VIII, and we see that they are now "normal," i.e., they are consistent with standard repulsive dominated nearest-neighbor potentials (in particular, A_1 is negative). Figures 16 and 17 compare the predicted QD model and pure-crystal harmonic A_{1g} and E_g2 stress-induced displacements, respectively. Inspection of Fig. 17(b) reveals that the (100)-(200) separation actually increases under an E_g symmetry stress, in contrast with the separation decrease exemplified by the pure-crystal displacements shown in Fig. 17(a) and the (δ_1,δ_2) model displacements given in Ref. 16. Notice that no such increase is seen for the QD model A_{1g} symmetry strains. Our predicted E_g symmetry stress-induced increase in the (100)-(200) separation means that a normal fit value of the (100)-(200) anharmonicity ($A_1<0$) produces a weakened (100)-(200) force constant, and this weakening partially cancels the stress-induced stiff-

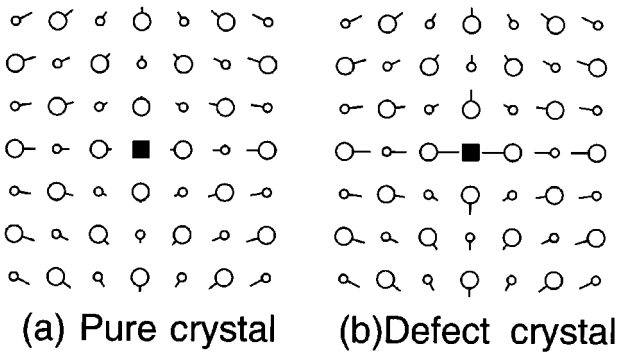

FIG. 17. Calculated KI:Ag^+ stress-induced E_g2 symmetry displacements in the x-y plane for (a) the pure crystal and (b) the QD model. Displacements for only one of the two E_g partners are shown, and the pure-crystal and defect-crystal strains are plotted to the same scale. The displacements are linear in the applied stress, and the scale was chosen to show the displacement pattern clearly. As for Fig. 16, the stress-induced displacements shown here are drawn with respect to the pure host-crystal equilibrium positions. Notice in (b) that the (200)-(100) separation actually *increases* under stress. When coupled with normal repulsive-dominated anharmonicity, this is consistent with the experimental observation of a small pocket-gap-mode E_g-stress coupling coefficient, as discussed in the text.

ening of other force constants, leading to the small E_g stress coupling seen experimentally for the T_{1u} pocket gap mode. In contrast, the (δ_1,δ_2) and $(\delta_1,\delta_2,\delta_3)$ models could only account for the necessary stress-induced force-constant weakening by using an unphysical fit value ($A_1>0$) for the cubic anharmonicity.

Figure 18 shows the E-field-induced mixing predicted by the QD model for a [100] applied E field of 87 kV/cm. The QD model predicted first-order mixing and frequency shifts for these modes are orders of magnitude smaller than for the (δ_1,δ_2) model.

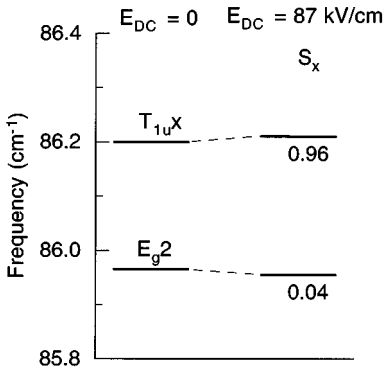

FIG. 18. QD model predicted mixing of the nearly degenerate A_{1g}, E_g2, and $T_{1u}x$ pocket gap modes in KI:Ag^+, under an applied 87 kV/cm E_{dc}[100] static E field. The S_x fractions give the strengths of the $\hat{x}$-polarized absorption relative to the zero-field absorption, and the dashed lines connect the zero-field modes with the mixed modes that they evolve into as the field magnitude varies from zero to 87 kV/cm. The predicted mixing for the A_{1g} symmetry pocket gap mode at 87.8 cm^{-1} is an order of magnitude smaller than the mixing shown here for the T_{1u} and E_g symmetry modes.

The mixing effects predicted for the pocket gap mode by the QD model are in fact so small that higher-order effects are important, as we have already anticipated. In particular, we find that the QD model $\sim E_{dc}^2$ cubic-cubic pocket-gap-mode frequency shifts are comparable to those obtained from the first-order E-field-induced mixing. In the Appendix, it is shown that the second-order E-field-induced displacements, which give rise to the cubic-cubic shifts, are given by [Eq. (A26)]

$$\xi_\alpha^2(n)=-\frac{1}{2}\sum_{m\beta l\gamma k\lambda} G_{\alpha\beta}(nm)\Phi_{\beta\gamma\lambda}(mlk)\xi_\gamma^{(1)}(l)\xi_\lambda^{(1)}(k), \tag{1}$$

where the $\{\xi_\alpha^{(1)}(m)\}$ appearing on the right-hand side of this equation are the defect-crystal first-order E-field-induced displacements determined from the harmonic theory and the $\{G_{\alpha\beta}(mn)\}$ are zero-frequency harmonic Green's-function elements for the defect lattice. Equation (1) formally resembles a harmonic response problem, with forces determined by sums over the products of the first-order E-field-induced displacements multiplied by the cubic anharmonic coefficients. Indeed, as shown in the Appendix, once we have found these ''effective forces'' using calculated first-order displacements and stress-fit cubic anharmonic coefficients, we can determine the pure-crystal harmonic displacements induced by these forces using pure-crystal zero-frequency Green's functions. These pure-crystal displacements are then converted into defect-crystal cubic-cubic displacements $\boldsymbol{\xi}^{(2)}$ needed to calculate the defect-crystal cubic-cubic shifts, following the same procedure we used to convert pure-crystal first-order E-field-induced displacements into defect-crystal first-order displacements. Note that the determination of the pure-crystal displacements from the effective forces is simply a formal procedure used to simplify our calculation of the defect-crystal displacements. In particular, this approach allows us to easily adapt the numerical machinery we have developed to solve the stress problem in Ref. 16 to this cubic-cubic problem, which has the same symmetry properties as the stress problem.

The first-order E-field-induced displacements predicted for the QD model are very similar to the (δ_1,δ_2) model displacements, in that for both models the E-field-induced displacements near the defect are an order of magnitude larger than the displacements farther out in the lattice. This suggests that the effective forces which produce the second-order displacements in the neighborhood of the defect, as described above, will be determined primarily by the large first-order displacements near the defect. Indeed, we find in our calculations that, for an applied [100] E field, the effective force on the (100) site is nearly two orders of magnitude larger than the effective forces on the other sites we considered. In order to determine these effective forces, we assumed nearest-neighbor cubic anharmonicity derivable from central potentials, as we did in the first-order calculation. However, the calculation of the effective force on the (100) site involves the (000)-(100) longitudinal cubic anharmonic coefficient $A_0=\Phi_{xxx}(000,000,100)$, and our pocket-gap-mode stress fits do not determine this cubic anharmonic coefficient. A similar calculation for the 17.3 cm^{-1} T_{1u} *resonant* mode, whose displacement pattern is strongly peaked

TABLE IX. Anharmonic parameters determined from the KI:Ag^+ T_{1u} resonant mode stress coupling coefficients, A, B, and C, measured in Ref. 3. Stress-fit anharmonicities determined from the three harmonic defect models discussed in the text are given. The values for the anharmonicities A_2 and A_3 from the pocket-gap-mode stress fits are included in the calculation; neglecting these pocket-mode stress-fit terms changes the stress-fit values listed here by roughly 10%. The units are 10^{12} dyn/cm^2.

Model	A_0	A_1	B_0
(δ_1,δ_2)	34 ±15	−95±37	0.14±0.09
$(\delta_1,\delta_2,\delta_3)$	−4±1	121±79	0.06±0.04
QD	−1.4±0.3	−14±23	0.06±0.04

on the defect site, can give us this anharmonicity. The results of such a calculation are given in Table IX, where we have fit the anharmonic coefficients $A_0=\Phi_{xxx}(000,000,100)$, $A_1=\Phi_{xxx}(100,100,200)$, and $B_0=\Phi_{xyx}(000,000,010)$ to the measured KI:Ag^+ 17.3 cm^{-1} T_{1u} resonant mode stress coupling coefficients given in Ref. 3. For comparison, we have also reported the results of similar calculations using the (δ_1,δ_2) and $(\delta_1,\delta_2,\delta_3)$ models. The A_1 coefficient used in this fit was also used in the pocket-gap-mode stress fit. Comparing the results in Table IX to the pocket-mode stress fits given in Table VIII, we see that, within the uncertainties, the QD model is the only model which produces consistent gap and resonant mode stress-fit values for A_1.

Returning to the cubic-cubic calculation, we were able to calculate the effective forces produced by an $E_{\rm dc}$ [100] field for the (±100), (±200), (±300), (0±10), and (00±1) sites by using the resonant and pocket-mode stress-fit anharmonicities listed in Tables VIII and IX. (For A_1, we used the pocket-mode stress-fit values of Table VIII.) Even though the effective forces on the (±200), (±300) sites are much smaller than the (±100) effective force, we included these forces in our calculation because they are close to the pockets where the gap modes have large displacements. We included the (0±10), (00±1) effective forces because they directly act upon ions affected by the QD force constant, and we have found these forces to be significant for determining the $E_{\rm IR}\perp E_{\rm dc}$[100] shifts.

For the same E field considered in Fig. 18, the predicted cubic-cubic $T_{1u}x$ mode shift is 0.009 cm^{-1}, which is comparable to the first-order shift shown in Fig. 18. In comparison, using quartic anharmonicities estimated from a Coulomb plus Born-Mayer potential fit to the harmonic parameters of the QD model, the second-order quartic anharmonic Stark-effect shift predicted for this same field is 0.003 cm^{-1}. This is a significant fraction of our cubic-cubic shift, but, since we do not have better estimates of the quartic anharmonicities needed to determine this shift, we are going to omit it from our calculations, keeping in mind that this neglected term might produce a slight increase in our overall predicted shifts.

Figure 15(c) compares the measured E-field-induced difference spectrum to the spectrum predicted by our QD model using our QD model stress-fit anharmonicities. The calculated difference spectrum includes both first-order mixing and second-order cubic-cubic shifts. The QD model results are a vast improvement over the (δ_1,δ_2) and $(\delta_1,\delta_2,\delta_3)$ model

TABLE X. Measured and QD model predicted E-field-induced frequency shifts for the T_{1u} pocket gap mode. The values in parentheses give the predicted minimum and maximum shifts produced by anharmonic parameters consistent with the uncertainties in the measured T_{1u} gap and resonant mode uniaxial stress coefficients.

$E_{\rm dc}$	$E_{\rm IR}$		$\Delta\omega/\Delta E^2$ [10^{-6} cm^{-1}/(kV/cm)^2]
[100]	[100]	Experiment	1.70±0.09
		QD model	1.13 (0.67/1.67)
[100]	[010]	Experiment	−0.93±0.05
		QD model	−0.42 (−0.28/−0.58)
[110]	[110]	Experiment	0.08±0.36
		QD model	0.32 (0.12/0.54)
[110]	[$\bar{1}$10]	Experiment	0.20±0.29
		QD model	0.39 (0.27/0.55)

predictions given in Figs. 15(a) and 15(b). The measured and computed shifts corresponding to the difference spectra in Fig. 15(c) are listed in Table X, along with shifts for other probe-field geometries. Note that these predictions are given directly by the theory, with no line-shape assumptions needed. The computed shifts are determined from strength-weighted frequency averages, $\bar{\omega}\equiv\Sigma_i S_i\omega_i/\Sigma_i S_i$, as a function of applied E-field strength. Of course, only field-induced IR-active modes near the 86.2-cm^{-1} mode are included in the average, since the small contribution to the predicted difference spectra from these modes strongly overlaps with the 86.2-cm^{-1} contribution. Thus, for example, we included the field-induced IR-active E_g gap mode near 86.0 cm^{-1}, when it appears, in our averages, but did not include the field-induced A_{1g} mode at 87.8 cm^{-1}. Over the range of field strengths attained in the present study, our predicted QD model shifts are found to be quadratic in the field to within 1%, despite the mixing and in agreement with the experimental results. This is not surprising considering that the cubic-cubic mechanism taken alone gives frequency shifts which are purely quadratic in the field, and the mixing mechanism alone gives an approximately quadratic dependence for sufficiently small fields, such as those considered here. The uncertainties in the predicted shifts given in Table X arise from uncertainties in the stress measurements, which are propagated through our calculations via the computed uncertainties in the stress-fit anharmonicities. The predicted and measured shifts for the $E_{\rm IR}\|E_{\rm dc}$[100] probe-field geometry are seen to overlap, while the predicted shift for $E_{\rm IR}\perp E_{\rm dc}$[100] is half the measured shift. The predicted and measured shifts for $E_{\rm dc}$[110] also overlap, but the uncertainty in the measured shifts for this field direction precludes strong conclusions. The corresponding shifts for the isotope pocket gap mode are given in Table XI, and we see that the predicted and measured values for this mode are also in good agreement.

As mentioned above, we neglected the second-order shifts produced by quartic anharmonicity. For the $E_{\rm IR}\|E_{\rm dc}$[100] shifts given in Table X, the estimated quartic anharmonic shift is roughly 1/3 of the predicted shift, so including this shift could slightly improve the agreement between the predicted and measured shifts. In contrast, the quartic anharmonic shift for the $E_{\rm IR}\perp E_{\rm dc}$[100] probe-field geometry is two orders of magnitude smaller than the shift given in Table X.

TABLE XI. Measured and QD model predicted E-field-induced frequency shifts for the isotope pocket gap mode. The values in parentheses give the predicted minimum and maximum shifts produced by anharmonic parameters consistent with the uncertainties in the measured T_{1u} gap and resonant mode uniaxial stress coefficients.

E_{dc}	E_{IR}		$\Delta\omega/\Delta E^2$ [10^{-6} cm^{-1}/(kV/cm)^2]
[100]	[100]	Experiment	1.13±0.10
		QD model	1.14 (0.79/1.60)
[100]	[010]	Experiment	−1.11±0.08
		QD model	−0.38 (−0.25/−0.53)
[110]	[110]	Experiment	−0.25±0.46
		QD model	0.38 (0.27/0.53)
[110]	[$\bar{1}$10]	Experiment	0.17±0.20
		QD model	0.38 (0.27/0.53)

Furthermore, there is no mixing predicted for this geometry and, hence, the $E_{IR}\perp E_{dc}[100]$ shift is *solely* a cubic-cubic effect. The measured pocket gap mode $E_{IR}\perp E_{dc}[100]$ shift is very unusual in that no other gap or resonant mode has ever been reported with a frequency shift for this probe field geometry. If we set our quadrupolar force constant change to zero when determining the cubic-cubic displacements from the effective forces, we find that the resulting $E_{IR}\perp E_{dc}[100]$ shift is a factor of 4 smaller than the shift predicted with the silver ion QD force-constant change included. Hence, we see that the silver ion QD also plays an essential role in producing this unusual $E_{IR}\perp E_{dc}[100]$ field-induced shift.

D. Resonant mode electric-field-induced shifts and mixing

Using the resonant mode stress-fit QD anharmonicities A_0 and B_0 given in Table IX (again taking A_1 from Table VIII), together with our calculated first-order E-field-induced strains and resonant mode displacement patterns, we can predict the T_{1u} and E_g low-frequency *resonant* mode E-field-induced mixing. In Fig. 19, the results of this calculation are compared with the mixing measured by Kirby.[4,5] The predicted and measured shifts are found to be in excellent agreement for all four defect/probe geometries considered by Kirby. It is worth noting that the measured 17.3-cm^{-1} mode frequency shifts for $E_{IR}\|E_{dc}[100]$ are consistently slightly smaller than the predicted shifts. This might indicate that the T_{1u} mode is being mixed with another mode to produce one of the weak E-field-induced IR-active modes seen by Kirby at frequencies above 20 cm^{-1}. However, the slight disagreement between theory and experiment seen in Fig. 19(a) is too small to draw any conclusions on this point.

It is instructive to extend our predictions for the gap-mode mixing beyond the maximum field strengths attained here. The solid and dashed curves in Fig. 20(a) show the predicted frequencies for the $T_{1u}x$ and E_g2 pocket gap modes as a function of the dc field strength for an $E_{IR}\|E_{dc}[100]$ geometry. For comparison, the experimentally measured IR frequencies for the pocket gap mode are included as squares. Notice that the experimental points lie very slightly below the predicted $T_{1u}x$ frequencies. However, as discussed in Sec. III C and just below, the predicted $T_{1u}x$ frequency shifts alone do not determine the observable frequencies, owing to

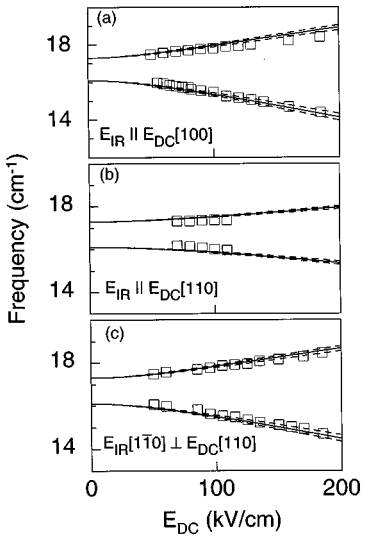

FIG. 19. Comparison between the QD model predicted and the measured E-field-induced $T_{1u}-E_g$ resonant-mode mixing for KI:Ag$^+$. This figure plots the mode frequencies as a function of applied field for (a) $E_{IR}\|E_{dc}[100]$, (b) $E_{IR}\|E_{dc}[110]$, and (c) $E_{IR}[110]\perp E_{dc}[110]$. The symbols give the frequencies measured in Ref. 5, while the solid curves are the QD model predictions and the dashed curves encompass the range of predicted shifts consistent with the uncertainties in the stress-fit anharmonicities. No shifts are predicted or measured for the $E_{IR}[001]\perp E_{dc}[110]$ field-probe geometry. The higher frequency mode in these figures becomes the IR-active T_{1u} resonant mode at zero field, and the lower frequency mode becomes the E_g resonant mode, which is field-induced IR-active for nonzero fields due to mixing with the T_{1u} mode.

the experimental linewidth, the smallness of the shifts, and the mode mixing produced by the applied field. The application of the static field mixes the $T_{1u}x$ and E_g2 modes, so that the E_g2 mode acquires some $T_{1u}x$ character and becomes field-induced IR active. This is shown in Fig. 20(b), which plots the predicted IR strengths for the mixed modes as a function of dc field strength. As the magnitude of the dc field increases, the "E_g2" mode (named for its symmetry at zero applied field) is seen to gain strength from the "$T_{1u}x$" mode, due to the mixing. Because of the relatively large experimental pocket-mode linewidth (0.5 cm^{-1} FWHM), the mixing and frequency separation of the two modes for the applied field strengths used in our experiments are sufficiently small that the mixing effects and mode shifts are not separately resolvable. This is clearly shown in Fig. 15(c). For such a small-mixing case, it is appropriate to use a strength-weighted frequency average in order to compare the predicted frequency shifts to the experimental shifts. Doing this brings the predicted shifts into better agreement with the experimental shifts shown in Fig. 20(a). At the largest fields shown in Fig. 20, the predicted $T_{1u}x-E_g2$ mixing increases dramatically. For example, at $E_{dc}=500$ kV/cm, the theoretical E_g2 mode strength is nearly one third of the $T_{1u}x$ strength. Our QD model predicts that for such large fields, the field-induced IR-active "E_g2" mode should be readily observable.

IV. DISCUSSION

It is interesting to compare the E-field-induced frequency shifts of the gap modes, presented in this paper, with the

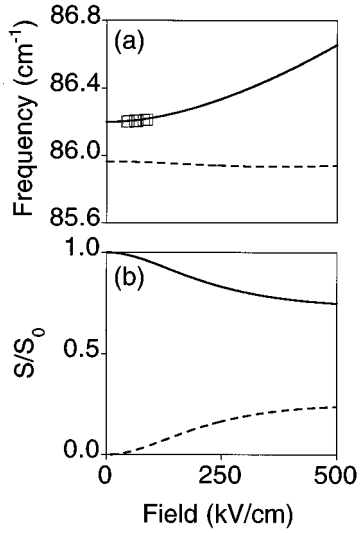

FIG. 20. Predicted frequencies (a) and relative strengths (b) for $T_{1u}x$ and E_g 2 pocket gap modes in KI:Ag^+, as a function of the dc field strength for an $E_{IR}\|E_{dc}[100]$ probe/field geometry. For comparison the measured pocket-mode frequencies are given by the squares in panel (a). The curves in panel (b) give the predicted IR strengths relative to the zero-field $T_{1u}x$ strength. In both panels the solid curves are for the $T_{1u}x$ mode, while the dashed curves are for the E_g2 mode. The (b) panel shows clearly how the E_g2 mode gains strength with increasing applied field as this mode acquires partial $T_{1u}x$ character, as discussed in the text. Notice that the range of applied field strength in this figure extends well beyond that of the highest E field used in our experiments. At these high fields, the E_g2 pocket gap mode is predicted to acquire sufficient IR strength that it should be separately observable in the spectra. This is unlike the case for the smaller fields used here, where the $T_{1u}x$ and E_g2 modes remain sufficiently close that they are not separately resolvable within the relatively large experimental pocket-mode linewidth ($\sim$0.5 cm^{-1} FWHM). The applied static field should also mix the A_{1g} pocket gap mode with the $T_{1u}x$ and E_g2 modes, but even for the highest field shown above, this mixing produces a field-induced IR-active A_{1g} mode having only a 2% strength relative to that of the zero-field $T_{1u}x$ mode. Accordingly, the A_{1g} mode has not been included in this figure.

E-field-induced shifts measured previously for resonant modes: the frequency shifts of the KI:Ag^+ and KI:Cl^- gap modes are at least two orders of magnitude smaller than that of the T_{1u} resonant modes of KI:Ag^+ (Ref. 5) and of NaI:Cl^-,[29] for the same applied field. Previously, some resonant mode systems, such as NaCl:Cu^+ and KBr:Li^+, were also found to exhibit very small E-field effects, perhaps within an order of magnitude of the gap-mode results; however, those measurements were not accurate enough to permit a detailed comparison with the gap mode.[29] In addition, the gap modes of Cs^+ and Rb^+ in KI show no E-field shift at all within our experimental precision. In contrast, the uniaxial stress coupling coefficients are comparable for both the gap and resonant modes of the same system.[16] Note that from a purely experimental point of view, for the gap modes studied in this work the frequency shifts at the maximum sustainable dc E field are 1–2 orders of magnitude smaller than the shifts measured at the maximum sustainable uniaxial stress;[16] this comparison points out the different levels of difficulty associated with these two experiments.

The Stark effect observed in the course of this work for the KI:Ag^+ pocket-gap modes is unusual in additional respects. First, Ag^+ appears to be the only substitutional cation defect whose gap modes show *any* measurable E-field-induced shifts. Second, even though small, the KI:Ag^+ pocket-gap-mode E-field-induced shifts are significantly larger than any other E-field effect measured for gap modes due to other impurities, such as those due to substitutional anion defects, e.g., Cl^- and Br^- in KI. Finally, the shifts of the Ag^+ pocket-gap modes for $E_{IR}\perp E_{dc}[100]$ are fairly unique in that only one of the previously measured resonant modes, due to KBr:Li^+, showed *any* E-field effect in this polarization;[29] even those other gap modes which were found to have small shifts for $E_{IR}\|E_{dc}[100]$ in the course of this work (e.g., Cl^-) show *no* effect for $E_{IR}\perp E_{dc}[100]$, qualitatively similar to the case of the resonant modes.

Although very small at the maximum fields sustainable in the present apparatus, intriguing effects were found for both the Cl^- and Br^- gap modes in KI. For Cl^-, it is surprising (1) that the two stronger gap modes due to the two naturally occurring Cl^- isotopes have such different E-field-induced shifts, and (2) that the weak mode identified previously as arising from a perturbation of the strong isotopically split doublet by the presence of host-$^{41}K^+$ isotopes has a much larger E-field-induced shift than the unperturbed doublet due to the two Cl^- isotopes only. It is unfortunate that this mode is so weak that its E-field effect is difficult to measure in samples with only natural abundances of the various K^+ and Cl^- isotopes; similar experiments on KI:Cl^- samples with isotopically pure Cl^- might serve to clarify the situation. For Br^-, the two members of what appeared originally to be a simple isotopically split doublet (due to the two naturally occurring Br^- isotopes) also behave ''anomalously'' under an applied dc E field, suggesting that these modes may, in fact, involve another defect, which would be consistent with the low absorption strength per impurity compared to other substitutional defect systems and also with the fact that the two lines shift in opposite directions with applied E field.

As noted, the QD model results for KI:Ag^+ are a vast improvement over the (δ_1,δ_2) and $(\delta_1,\delta_2,\delta_3)$ model predictions. Not only is the QD model able to provide a consistent explanation for the pocket-gap-mode stress and E-field measurements, but it also predicts a large E-field-induced mixing for the T_{1u} and E_g resonant modes, in excellent agreement with the experimental results. Thus, the QD model has passed a stringent test by providing a consistent explanation for these dramatically different gap and resonant mode E-field-induced shifts, together with the unusual gap-mode stress shifts reported previously.[16] Note that *none* of the parameters used in the QD model were adjusted to produce this agreement. The harmonic parameters were all fit to the measured zero-field, zero-stress IR-absorption and Raman-scattering spectra, while the anharmonic parameters were fit solely to the stress data. The QD model also significantly improves upon most of the original (δ_1,δ_2) model harmonic predictions; those properties which are not improved remain the same. Finally, the QD model provides a natural explanation for the unusual KI:Ag^+ gap-mode stress behavior in terms of unusual E_g symmetry strains, rather than anomalous host-ion nearest-neighbor cubic anharmonicities. A full summary of the experimental data and the agreement and dis-

agreement obtained for the three different models is presented in Table XII; the first 11 items compare the low-temperature experimental results with the harmonic approximation, while items 12–17 include anharmonic contributions.

We should mention that, besides the $(\delta_1,\delta_2,\delta_3)$ and QD models, we have also considered a QD model without δ_3. This model also predicted pocket-gap mode E-field-induced shifts that differed dramatically from the measured shifts. Thus *both* the Ag^+ quadrupolar deformability and the extended relaxation-induced force-constant change δ_3 are essential features of our model. Models that also failed badly included those employing other force-constant changes, such as iodine-iodine second-neighbor longitudinal, (000)-(010) transverse, (100)-(110) transverse, and three-body van der Waals interactions.[42] Most of these alternative models reproduced neither the position of the low-frequency E_g resonant mode nor the unusual E_g symmetry strains necessary to bring the pocket-gap-mode stress and E-field results into agreement, without giving up the fit to the measured IR-resonant and gap-mode frequencies. Those models with force-constant changes which came close to reproducing the pocket-gap-mode stress and E-field results without ruining the IR fit had other serious drawbacks, such as additional, unobserved absorption peaks in their predicted IR spectra. The successes of our QD model and the failures of these alternatives demonstrate that the silver ion possesses a significant electronic quadrupolar deformability in the KI:Ag^+ system and that this deformability plays an essential dynamical role.

The simultaneous presence of the pocket-gap modes, with displacements patterns peaked away from the defect, and the low-frequency resonant modes, with displacements peaked at the defect and its nearest neighbors, has allowed us to determine the anharmonicity between host ions in the lattice as well as between the defect and its nearest neighbors. This has been done by fitting nearest-neighbor cubic anharmonicities to measured uniaxial stress-induced frequency shifts, and these have led to predicted E-field shifts in accord with experiment. The anharmonicity results for our QD model, listed in Tables VIII and IX, are qualitatively comparable to the Born-Mayer values listed in the fourth row of Table VIII. Hence, we have found no evidence of anomalously strong anharmonicity in this system. Of course, it is essential to consider the ratio of anharmonic to harmonic terms in order to determine the importance of the anharmonic effects, and our QD model predicts substantial harmonic softening for the KI:Ag^+ on-center system. This softening might enhance the relative importance of the anharmonicity for the KI:Ag^+ dynamics beyond that suggested by the magnitude of the stress-fit anharmonicities.

V. CONCLUSIONS

This study originally was an attempt to learn more about the anomalous thermally driven KI:Ag^+ on-center to off-center transformation by modeling the low-temperature, on-center dynamics. In particular, we were interested in reconciling the fact that the KI:Ag^+ on-center dynamics appear to be well described by a perturbed harmonic model, whereas the system's observed thermal instability suggests the presence of strong anharmonicity. We were looking for behavior which could not be explained by a standard quasiharmonic defect model, which treats the anharmonicity as a perturbation. Indeed, given that measurements for several of the on-center configuration anharmonic properties are very unusual, such as the measured pocket-gap-mode stress and E-field-induced frequency shifts, it was not obvious *a priori* that a successful quasiharmonic model could be constructed for the on-center dynamics. However, the QD model has been shown here to account naturally for these unusual anharmonic properties within a quasiharmonic framework that uses normal anharmonicities and the unusual E_g symmetry stress-induced strains near the (200) family of pockets predicted by our harmonic model. Besides the Ag^+ QD force-constant change, the model also includes relaxation-induced force-constant changes (δ_3) beyond those already contained in the original (δ_1,δ_2) model; nevertheless, these relaxation-induced force-constant changes are computed without the addition of any harmonic parameters beyond those already contained in the model, namely, δ_1, δ_2, and δ_{QD}.

The QD force-constant change δ_{QD} corresponds physically to vibrationally induced deformations of the Ag^+ electronic charge cloud, of quadrupolar symmetry. As noted earlier, δ_{QD} arises quantum mechanically from virtual s-d electronic transitions, and it couples exclusively to perturbed modes of E_g symmetry. Thus both the 16.1 cm^{-1} E_g resonant mode and the E_g stress-induced static displacements, which were not well described in our previous models, are strongly affected by δ_{QD}. This is the key element of the QD model's success.

The QD model not only provides a consistent explanation for the pocket-mode stress and E-field measurements, but, as indicated in Table XII, it also reproduces many of the other on-center configuration measurements as well; as a result 25 pieces of experimental data are described with eight theoretical parameters, within experimental errors. However, there are a few exceptions (see Table XII): the pocket-gap-mode/isotope-gap-mode relative strength (item 6), the absolute strength of the pocket gap mode (item 8), the absolute strength of the impurity-induced T_{1u} spectrum (item 9), the fine structure in the acoustic spectrum (item 10), one of the pocket-gap-mode E-field measurements (item 14), and one of the isotope pocket-gap-mode E-field measurements (item 15). Nevertheless, the fits are remarkably good considering that several alternative models do not come even remotely close to reproducing these results. In particular, none of the alternative models could consistently account for both the unusual pocket-gap-mode stress and E-field-induced frequency shifts without seriously compromising their fits to the low-temperature IR and Raman spectra. In fact, using pocket-mode stress anharmonicities, most of the alternative models predict pocket-gap-mode E-field-induced shifts two orders of magnitude larger than the observed shifts. The success of our QD model, combined with the dramatic failures of these alternative models, convincingly demonstrates that the QD model correctly describes the on-center dynamics of KI:Ag^+. The model's success, then, actually deepens the mystery surrounding the anomalous on/off center thermal instability by showing that this system's $T=0$ K on-center dynamics are well described by a quasiharmonic model, albeit

TABLE XII. Comparison of the KI:Ag^+ on-center experimental results with calculated results based on perturbed shell models. (a) the two-harmonic-parameter (δ_1,δ_2) model; (b) the two-harmonic-parameter ($\delta_1,\delta_2,\delta_3$) model, and (c) the three-harmonic-parameter QD model.

Experimental results (Ref.)		SM results		
		(a) Harmonic approx.	(b) Harmonic approx.	(c) Harmonic approx. $\delta_1=-\Delta\Phi_{xx}(000,100)$ $\delta_2=-\Delta\Phi_{xx}(100,200)$ $\delta_{QD}=\Delta\Phi_{xx}(100,-100)$ $=2\Delta\Phi_{xy}(100,010)$
1.	T_{1u} resonant and gap mode freqs. (17.3 cm^{-1}, 86.2 cm^{-1}) (Refs. 1 and 5)	Fit to 2-param. (δ_1,δ_2) model	Fit to 2-param. ($\delta_1,\delta_2,\delta_3$) model	Fit in 3-param. QD model
2.	E_g resonant mode (16.1 cm^{-1}) (Refs. 5 and 7)	Fair agreement (20.5 cm^{-1})	Poor agreement (26.3 cm^{-1})	Fit in 3-param. QD model
3.	Relative T_{1u} gap/resonant mode strengths (~3) (Refs. 5–7)	Fair agreement (1.4)	Good agreement (3.0)	Good agreement (3.0)
4.	Resonant mode isotope frequency shift (-0.14 ± 0.03) (Ref. 2)	Poor agreement (-0.05)	Good agreement (-0.12)	Good agreement (-0.12)
5.	Gap mode isotope frequency shift (-1.7) (Ref. 17)	Good agreement (-1.46)	Good agreement (-1.63)	Good agreement (-1.64)
6.	Relative gap mode isotope strength (0.04) (Refs. 8 and 17)	Fair agreement (0.073)	Fair agreement (0.074)	Fair agreement (0.073)
7.	A_{1g} resonant mode not observed (Refs. 5 and 7)	A_{1g} resonant mode (37.3 cm^{-1})	A_{1g} resonant mode (41.5 cm^{-1})	A_{1g} resonant mode (41.5 cm^{-1})
8.	Absolute T_{1u} gap mode strength (theory/experiment) (Ref. 6) (Ag+/Ag concentration ratio in the crystal is not known.)	Poor agreement (7)	Poor agreement (10)	Poor agreement (10)
9.	Strength of the broad acoustic T_{1u} absorption spectrum (Ref. 8)	Poor agreement	Poor agreement	Poor agreement
10.	Weak absorption peaks at 30, 44, 55.8, and 63.6 cm^{-1} (Refs. 5, 6, and 8)	Poor agreement	Poor agreement	Poor agreement
11.	A_{1g} and E_g gap modes not observed in Raman (Ref. 7)	Predicts A_{1g} and E_g pocket modes with negligible Raman strengths. (87.2 cm^{-1}, 86.0 cm^{-1})	Same	Same
		Stress and electric field dependence		
				Anharmonic QD model $A_0=\Phi_{xxx}(000,000,100)$ $A_1=\Phi_{xxx}(100,100,200)$ $A_2=\Phi_{xxx}(200,200,300)$ $B_0=\Phi_{xyx}(000,000,010)$ $B_1=\Phi_{yxy}(100,100,200)$
12.	T_{1u} pocket gap mode and resonant mode stress effect (Refs. 3 and 16)			Five parameter fit to the Anharmonic QD model
13.	Isotope pocket mode stress effect (Ref. 16)			Good agreement
14.	Pocket-gap-mode Stark effect			Data agree with predictions of the QD model using stress-fit anharmonicities (with no additional parameters)
15.	Isotope pocket-mode Stark effect			Good agreement
16.	Stark effect for T_{1u} and E_g resonant modes (Ref. 5)			Excellent agreement
17.	Large gap mode linewidth in comparison to other gap mode systems (0.5 $cm^{-1}\leftrightarrow$0.14 cm^{-1}) (Ref. 16)			Outside of the model

TABLE XII. (*Continued*).

Experimental results (Ref.)	SM results
Temperature dependence	
Observations (with increasing temperature)	Temperature-dependent properties are outside the framework of the anharmonic QD model
18. Disappearance of the T_{1u} and E_g resonant and T_{1u} pocket-mode strengths (Refs. 6, 7, and 11)	
19. Weak broad IR gap mode (78.6 cm^{-1}) appears and then levels off (Ref. 6)	
20. Raman resonant mode ($A_{1g}+E_g$) (12.2 cm^{-1}) appears and then disappears (Ref. 7)	
21. Temperature-dependent pocket gap mode A and B stress coefficients (Ref. 16)	

a model which has revealed some fascinating unexpected behavior.

Table XII also lists experimental effects that are outside the framework of the $T=0$ K quasiharmonic model (items 18–21). A possibility raised by our results is that the on-center to off-center transformation might be related to the Ag^+ QD, which has been suggested[24] to play a role in determining the observed Ag^+ off-center configuration in the rubidium halides.[33,43–48] It remains to be seen whether the harmonic force-constant weakening, the Ag^+ QD or, possibly, a combination of both effects, plays an important role in the KI:Ag^+ on-center to off-center transformation.

Electronic quadrupolar deformability has also been proposed as an explanation for several of the unusual properties of silver halides.[21,23,25,41] In particular, calculations suggest that the Ag^+ QD is primarily responsible for the high mobility seen for the silver ion in AgCl and AgBr.[26,27] Moreover, the Ag^+ QD could also be responsible for the superionic conductivity seen in AgI.[25] However, these suggestions have been vigorously debated, and several alternate mechanisms have been proposed. For instance, a three-body van der Waals interaction has been suggested to account for phonon properties and strong Cauchy relation violations in AgCl and AgBr, previously attributed to the Ag^+ QD.[42] In addition, all of these calculations include many assumptions about the nature of interatomic potentials unrelated to the Ag^+ QD. Given the uncertainties associated with these auxiliary assumptions, the status of the Ag^+ QD as an important effect in these earlier studies is far from clear.

To compare our QD results with these earlier studies, we note that the value of our QD force-constant change $\delta_{\rm QD}$ for KI:Ag^+, reexpressed in terms of the Ag^+ QD parameter S_{E_g} used in Refs. 21–23 and 41, is $S_{E_g}=2\,\delta_{\rm QD}=2280$ dyn/cm. This is within the range of values determined from quantum-mechanical estimates of the Ag^+ QD for AgCl and AgBr,[41] or obtained from phenomenological shell model fits to the phonon spectra of these same crystals;[21–23] these values vary from $S_{E_g}=542$ dyn/cm (Ref. 22) to 2580 dyn/cm,[41] depending upon the additional assumptions that were made in the various models. A more quantitative comparison is unwarranted, because the Ag^+ QD force-constant change should depend on the strength of the overlap interaction between the Ag^+ defect and its nearest-neighbor halide ions,[24] which is quite different for the nearly unstable KI:Ag^+ on-center configuration and for the silver halides.

The above discussion highlights an important component of our combined detailed theoretical-experimental study. By means of a large number of experiments (IR, Raman, dielectric response, isotope, uniaxial stress, static E-field), and because of the complementary aspects of the low-frequency resonant modes and pocket gap modes in KI:Ag^+, which have allowed us to probe in great detail the anharmonicity *both* at the defect and in the host lattice near the (200) family of sites, we have been able to establish that the Ag^+ QD plays an essential role in the KI:Ag^+ dynamics. This in turn strongly supports the earlier suggestions that the Ag^+ electronic quadrupolar deformability is an important general feature in the dynamics of other host-silver systems and of silver halides.

ACKNOWLEDGMENTS

The help of C. E. Mungan with the data analysis software is gratefully acknowledged. The work by A.R., B.P.C., and A.J.S is supported by NSF-DMR-9312381 and ARO-DAAL03-92-G-0369. B.P.C. received additional support from NSERC of Canada. In addition, this research made use of the MRL Facilities supported by the National Science Foundation under Grant No. DMR-9121654. The work by K.W.S. and J.B.P. is supported by NSF-DMR-9014729 and NSF-DMR-9510182. J.B.P. gratefully acknowledges the support of the Alexander von Humboldt Foundation and the Institute for Theoretical Physics at the University of Regensburg, Germany during a portion of this work. K.W.S. thanks the Achievements Rewards for College Scientists for partial support during a portion of this work.

APPENDIX: ELECTRIC-FIELD SHIFT THEORY

In the main text, we gave a qualitative outline of how we extended our harmonic defect model in order to describe the dc E-field-induced frequency shifts for the pocket-gap modes. Here we present a more detailed discussion. Additional details for the theoretical calculations of this paper are given in Ref. 49.

In the presence of external forces, the equation of motion for N ions interacting via harmonic forces is

$$\mathbf{M}\ddot{\mathbf{u}}=-\mathbf{\Phi u}+\mathbf{F}_{\rm ext}, \tag{A1}$$

where $\mathbf{u}=\{u_\alpha(l)\}$ is the $3N$-dimensional vector containing the ion displacements from their equilibrium positions, $\mathbf{\Phi}=\{\Phi_{\alpha\beta}(lm)\}$ is the harmonic force-constant matrix, $\mathbf{M}=\{M_l\delta_{\alpha\beta}\}$ is the diagonal mass matrix, and $\mathbf{F}_{\rm ext}=\{(\mathbf{F}_{\rm ext})_\alpha(l)\}$ contains external forces acting upon each of the ions. Here, $l,m=1,\ldots,N$ label the ion sites, while $\alpha,\beta=x,y,z$ denote Cartesian components.

Our adaptation of the method of Ref. 39 to determine the defect-crystal response to an external E field exploits the fact that for a given applied field, the *external* forces acting upon the defect and pure crystal are identical. This will be the case provided we assume that the effective charges coupling the E field to the ions remain unchanged by the introduction of the defect. The first-order field-induced static displacements for the defect crystal, $\boldsymbol{\xi}^{(1)}$, can thus be related to the pure-crystal field-induced displacements, $\boldsymbol{\xi}_0^{(1)}$, by solving Eq. (A1) for the external forces and equating the resulting pure-crystal and defect-crystal expressions to yield

$$[\mathbf{\Phi}_0+\mathbf{C}(0)]\boldsymbol{\xi}^{(1)}=\mathbf{\Phi}_0\boldsymbol{\xi}_0^{(1)}, \tag{A2}$$

where the perturbing matrix, $\mathbf{C}(\omega^2)\equiv\Delta\mathbf{\Phi}-\omega^2\Delta\mathbf{M}$ is evaluated at zero frequency, since $\boldsymbol{\xi}^{(1)}$ and $\boldsymbol{\xi}_0^{(1)}$ are *static* displacements. Multiplying this equation on the left by the unperturbed crystal zero-frequency Green's function $\mathbf{G}_0(0)=\mathbf{\Phi}_0^{-1}$, yields the equation

$$[\mathbf{I}+\mathbf{G}_0(0)\mathbf{C}(0)]\boldsymbol{\xi}^{(1)}=\boldsymbol{\xi}_0^{(1)}. \tag{A3}$$

This can be partitioned into two equations involving quantities inside and outside the defect space, defined by the sites associated with nonzero elements of $\mathbf{C}$. The resulting equations are

$$\boldsymbol{\xi}_I^{(1)}=(\mathbf{I}_{II}+\mathbf{G}_{0II}\mathbf{C}_{II})^{-1}\boldsymbol{\xi}_{01}^{(1)}, \tag{A4}$$

and

$$\boldsymbol{\xi}_R^{(1)}=-\mathbf{G}_{0RI}\mathbf{C}_{II}\boldsymbol{\xi}_I^{(1)}+\boldsymbol{\xi}_{0R}^{(1)}, \tag{A5}$$

where the I and R subscripts refer to components inside and outside the defect space, respectively. If the defect space is small, which is usually the case for isoelectronic defects, one can readily solve Eq. (A4) to determine the defect-space ion displacements in terms of the pure-crystal field-induced displacements and the defect-space zero-frequency Green's function elements. Equation (A5) then determines the defect-crystal field-induced displacements outside the defect space. Due to the localized nature of the pocket gap modes, we need only a limited number of field-induced displacements outside the defect space to determine the E-field-induced frequency shifts.

In order to determine the Green's-function elements needed for Eqs. (A4) and (A5), the static Green's function can be rewritten as

$$\mathbf{G}_0(0)=\sum_f \boldsymbol{\chi}(f)\tilde{\boldsymbol{\chi}}(f)/\omega_f^2,$$

where $\boldsymbol{\chi}(f)$ is the normal mode displacement pattern for mode f normalized according to $\tilde{\boldsymbol{\chi}}(f)\mathbf{M}_0\boldsymbol{\chi}(f)=1$. For the pure crystal, the normal modes are conveniently taken as complex plane waves: $\chi_\alpha(lb|\mathbf{k}j)\propto e_\alpha(b|\mathbf{k}j)\exp[-i\mathbf{k}\cdot\mathbf{R}(lb)]$, where j denotes the polarization branch, $e_\alpha(b|\mathbf{k}j)$ is a polarization vector, $\mathbf{k}$ is the wave vector, and $\mathbf{R}(lb)$ is the equilibrium position for the (lb) ion. The preceding equation is then

$$\mathbf{G}_0(0)=\sum_{\mathbf{k}j} \boldsymbol{\chi}(\mathbf{k}j)\boldsymbol{\chi}^\dagger(\mathbf{k}j)/\omega_{\mathbf{k}j}^2, \tag{A6}$$

and a given Green's-function element, $G_{0\alpha\beta}(l,m)$, can be calculated by directly summing over the pure-crystal normal modes determined by the breathing shell model.

Before we can determine the defect-crystal response to an applied E field, we first need to know the pure-crystal response. In the static limit, we can determine the pure-crystal harmonic response, $\boldsymbol{\xi}_0^{(1)}$, to an external E field by multiplying Eq. (A1) on the left by the zero-frequency harmonic Green's function, $\mathbf{G}_0(\mathrm{O})$, which yields the expression

$$\boldsymbol{\xi}_0^{(1)}=\mathbf{G}_0(0)\mathbf{F}_{\rm ext}. \tag{A7}$$

Experimentally, one studies a crystal section inserted between two capacitor plates. In contrast, the shell model used in this paper is for an infinite crystal, with periodic boundary conditions. An apparent difference between the model and the experimental situation is the presence of polarization charges on the surface of the KI:Ag^+ dielectric. In our shell model, the external forces occurring in Eq. (A7) are those produced solely by charges *external* to the crystal, with the effects due to all of the internal charges included via the Green's function. The presence of the surface polarization charges in the experimental situation raises the question of whether we should treat the polarization charges as external charges when computing the field-induced displacements. However, it is a simple exercise in electrostatics to show that, for *both* the infinite crystal and the experimental finite slab geometry, the longitudinal static macroscopic field due to internal sources is given by $\mathbf{E}_{\rm int}^l=-4\pi\mathbf{P}^l$, where $\mathbf{P}^l$ is the longitudinal polarization. These are the appropriate quantities to compare because, as discussed in more detail below, the static E field is longitudinal in character. Hence for longitudinal static E fields, our infinite-lattice shell model corresponds to the finite slab geometry of the experiment, with no surface polarization corrections needed. As a result, when calculating the external forces $\mathbf{F}_{\rm ext}$ occurring in Eq. (A7), we need to include only the field due to external sources, i.e., the charges on the plates. Note that in the main body of the paper, $E_{\rm dc}$ always refers to the applied field determined by dividing the voltage difference measured across the metal plates by the plate separation. A standard electrostatic calculation shows that the external E field due to the charges on the plates is related to the applied field by $E_{\rm ext}=E_{\rm dc}/\epsilon_0$, where ϵ_0 is the pure-crystal dielectric constant.

If the ions within the pure crystal were truly rigid, the external force would be given by the equation

$$\mathbf{F}_{\rm ext}=\mathbf{Z}\mathbf{E}_{\rm ext}, \tag{A8}$$

where $\mathbf{E}_{\rm ext}=\{(\mathbf{E}_{\rm ext})_\alpha(l)\}$ is a $3N$-dimensional vector describing the external E field acting on each of the ions, and $\mathbf{Z}$ is a diagonal matrix containing ionic charges $Z_{\alpha\beta}(lm)=\pm q\delta_{\alpha\beta}\delta_{lm}$. Here q is the ionic charge and the $+(-)$ sign denotes a cation (anion) site. However, the ions are *not* rigid, and the electronic response to the external E field produces internal forces which modify this rigid-ion expression. The

electronic response can be included in Eq. (A8) by replacing the charge, q, appearing there by a *longitudinal* effective charge, q',[15] so-called because the applied static E field is longitudinal in character [see the discussion following Eq. (A14) below]. We calculated the value of this effective charge in two different ways, finding agreement to within 2%. First, we determined the effective charge fraction $Z_L \equiv q'/e$ via the phenomenological expression

$$Z_L = \left(\frac{\epsilon_0 - \epsilon_\infty}{\epsilon_0 \epsilon_\infty}\right)^{1/2} \left(\frac{\mu V_0}{4\pi e^2}\right)^{1/2} \omega_{\mathrm{LO}} \tag{A9}$$

obtained on p. 66 of Ref. 15. In this equation ϵ_0 and ϵ_∞ are the static and high-frequency dielectric constants, respectively, ω_{LO} is the longitudinal optic-mode frequency, V_0 is the unit-cell volume, and μ is the reduced mass for the ions in a unit cell. All of these quantities are for the host crystal, and when we substitute the values used in computing the KI breathing shell-model phonons[50] we obtain $Z_L \equiv 0.4081$. This value differs markedly from the total ionic charge $q = 0.9e$ in the KI breathing shell model. Accordingly, it is now clarifying to replace the phenomenological expression (A9) by a fully microscopic shell-model expression.

The shell model used to determine the pure KI phonons includes the electronic degrees of freedom explicitly. Each ion is described by a ''core,'' consisting of the nucleus plus the ion's tightly bound (unpolarizable) electrons, attached via an isotropic harmonic spring to a massless spherical shell, which describes the ion's polarizable electrons. The cores and shells of different ions then interact via short-range overlap harmonic forces and the harmonic part of their long-range Coulomb forces. The shells are massless in accordance with the Born-Oppenheimer approximation, so that their instantaneous equilibrium positions are determined by the instantaneous core positions plus any external forces that are present. For an applied static E field, the core and shell equations may be written as

$$\mathbf{X}\mathbf{E}_{\mathrm{ext}} = \mathbf{\Phi}_{cc}\boldsymbol{\xi}_{0Ec} + \mathbf{\Phi}_{cs}\boldsymbol{\xi}_{0Es}, \tag{A10}$$

$$\mathbf{Y}\mathbf{E}_{\mathrm{ext}} = \mathbf{\Phi}_{sc}\boldsymbol{\xi}_{0Ec} + \mathbf{\Phi}_{ss}\boldsymbol{\xi}_{0Es}, \tag{A11}$$

where the subscripts c and s denote core and shell displacements, $\mathbf{X}$ and $\mathbf{Y}$ are diagonal matrices containing the core and shell charges, respectively, and $\mathbf{E}_{\mathrm{ext}}$ is the applied external field. The sum $\mathbf{X}+\mathbf{Y}$ for each ion gives the ion's total charge. These equations can be reduced formally to an equation involving only the core displacements by solving Eq. (A11) for $\boldsymbol{\xi}_{0ES}$ and substituting the result into Eq. (A10). Doing this yields

$$\mathbf{\Phi}\boldsymbol{\xi}_{0Ec} = (-\mathbf{\Phi}_{cs}\mathbf{\Phi}_{ss}^{-1}\mathbf{Y} + \mathbf{X})\mathbf{E}_{\mathrm{ext}}, \tag{A12}$$

where the ion-ion ''formal'' force constant matrix is given by

$$\mathbf{\Phi} \equiv \mathbf{\Phi}_{cc} - \mathbf{\Phi}_{cs}\mathbf{\Phi}_{ss}^{-1}\mathbf{\Phi}_{sc}.$$

This is the effective ion-ion, or formal force-constant matrix which we have used throughout this paper. It should be noted that the breathing shell model used in this work also includes a ''breathing'' degree of freedom which describes adiabatic isotropic deformations of the ions' electron clouds. This additional electronic degree of freedom can also be eliminated, analogous to the above elimination of the shell degrees of freedom. For clarity, we are not explicitly discussing this additional degree of freedom here, although it has been included in our calculations.

Comparing Eq. (A12) with Eq. (A8), we see that the matrix containing the longitudinal effective charges coupling the ion (core) displacements to the E field is given by

$$\mathbf{Z}_L = -\mathbf{\Phi}_{cs}\mathbf{\Phi}_{ss}^{-1}\mathbf{Y} + \mathbf{X}. \tag{A13}$$

The periodic symmetry of the pure crystal reduces the $6N_c \times 6N_c$ normal mode problem to a 6×6 problem for each of the N_c phonon wave vectors, where N_c is the number of unit cells. Hence, the above longitudinal effective charges are readily determined from the KI breathing shell-model matrices for $\mathbf{\Phi}_{sc}$, $\mathbf{\Phi}_{cs}$, $\mathbf{Y}$, and $\mathbf{X}$. In this way we find that Eq. (A13) predicts the magnitude of the longitudinal effective charge to be

$$Z_L = 0.4033,$$

which differs by less than 2% from our earlier phenomenological result of Eq. (A9). For consistency, we used the above result of our shell-model longitudinal effective-charge calculation in all of the calculations of this paper.

Using the expression for $\mathbf{G}_0(0)$ given by Eq. (A6), we can rewrite Eq. (A7) as

$$\boldsymbol{\xi}_0^{(1)} = \sum_{\mathbf{k}j}{}' [\boldsymbol{\chi}(\mathbf{k}j)\boldsymbol{\chi}^{\dagger}(\mathbf{k}j)/\omega_{\mathbf{k}j}^2]\mathbf{Z}\mathbf{E}_{\mathrm{ext}}, \tag{A14}$$

where the sum excludes the three $\omega_t = 0$ uniform translational modes which do not contribute to the crystal response. Since the static field is uniform throughout the crystal, only the $\mathbf{k}=0$ modes give a nonzero contribution to the scalar product in Eq. (A14). We have three uniform translational modes, one longitudinal optic (LO) mode and two transverse optic (TO) modes, all with $\mathbf{k}=0$. As mentioned above, the translational modes clearly do not contribute to Eq. (A14), which leaves only the TO and LO modes as possible contributors. In the electrostatic approximation used to determine the unperturbed crystal modes, the $\mathbf{k}=0$ TO and LO displacement patterns are identical; hence, at first sight it appears that both of these modes might contribute equally to Eq. (A14). However, the situation changes when we consider the limiting case of a small, but nonzero $\mathbf{k}$. A static field slowly varying in space only has $\mathbf{k}$'s aligned parallel to the field direction; otherwise, $\nabla \times \mathbf{E} \neq 0$ and the field would no longer be static. Hence, such a field only couples to the LO modes. In the static uniform field limit, then, we should include only the $\mathbf{k}=0$ LO modes in the sum occurring in Eq. (A14), with the mode polarization vectors parallel to $\mathbf{E}$.

For simplicity, we now consider an external field directed along the $\hat{x}$ axis, $\mathbf{E} = E_{\mathrm{ext}}\,\hat{x}$. The $\hat{x}$-polarized LO-mode displacement pattern is thus given by

$$\chi_\alpha(l|\mathrm{LO}) = \pm\frac{\delta_{x\alpha}}{m_\pm}\sqrt{\frac{\mu}{N_c}}, \tag{A15}$$

where the $+(-)$ sign corresponds to a cation (anion) site, and $\mu \equiv m_+ m_-/(m_+ + m_-)$ is the reduced mass for the ions within the unit cell. Substituting this result into Eq. (A14) yields

$$\xi^{(1)}_{0\alpha}(l) = \pm \frac{\delta_{x\alpha}}{m_\pm} \frac{q' E_{\rm ext}}{\omega^2_{\rm LO}}. \tag{A16}$$

We will have similar results for external E fields directed along the $\hat{y}$ and $\hat{z}$ axes. Since superposition holds for the pure crystal harmonic response that we are calculating here, we can write in general

$$\xi^{(1)}_{0\alpha}(l) = \pm \frac{q'(E_{\rm ext})_\alpha}{m_\pm \omega^2_{\rm LO}}, \tag{A17}$$

where this equation relates the displacements directly to the external E field.

The first-order E-field-induced displacements are determined following the methods described above. To lowest order in these E-field-induced displacements, the corrections to the unperturbed defect-crystal force-constant changes are given by

$$\delta\Phi^1_{\alpha\beta}(lm) = \sum_{n\gamma} \Phi_{\alpha\beta\gamma}(lmn)\xi^{(1)}_\gamma(n), \tag{A18}$$

where the $\Phi_{\alpha\beta\gamma}(lmn)$ are the cubic anharmonic coefficients and the 1 superscript emphasizes that these are first-order quantities linear in the applied E field.

The nearly degenerate T_{lu}, E_g, and A_{lg} pocket modes can be mixed strongly by an applied E field, necessitating the use of nearly degenerate perturbation theory to calculate the E-field-induced frequency shifts for these modes. The nearly degenerate perturbation equations are

$$(\mathscr{B}_E - \mathbf{\Delta}\omega^2)\mathbf{a} = 0, \tag{A19}$$

where $\mathscr{B}_{E,f\,f'} = \tilde{\boldsymbol{\chi}}(f)\delta\mathbf{\Phi}^1\boldsymbol{\chi}(f')$ is the 6×6 matrix coupling the six degenerate pocket modes, and $\mathbf{\Delta}\omega^2$ gives the E-field-induced squared frequency shifts. The components of the eigenvector $\mathbf{a}$ determine the zeroth-order displacement patterns, $\boldsymbol{\psi}$, as linear combinations of the six nearly degenerate pocket modes: $\boldsymbol{\psi} = \Sigma_f a_f \boldsymbol{\chi}(f)$, where the index f denotes the pocket gap modes:

$$f = 1{:}T_{1u}x, \quad f = 2{:}T_{1u}y,$$

$$f = 3{:}T_{1u}z, \quad f = 4{:}E_g1,$$

$$f = 5{:}E_g2, \quad f = 6{:}A_{1g}.$$

The normalization condition $\tilde{\boldsymbol{\psi}}(i)\mathbf{M}\boldsymbol{\psi}(i) = 1$ implies that $\Sigma^6_{f=1} a^2_f(i) = 1$ for normalized $\boldsymbol{\chi}$'s.

Using standard group-theoretic symmetry arguments, it can be shown that the matrix $\mathscr{B}_E$ coupling the pocket gap modes can be written in general as

$$\mathscr{B} = \begin{pmatrix} 0 & 0 & 0 & 0 & B_{TE}E_x & B_{TA}E_x \\ 0 & 0 & 0 & \frac{\sqrt{3}}{2}B_{TE}E_y & -\frac{1}{2}B_{TE}E_y & B_{TA}E_y \\ 0 & 0 & 0 & -\frac{\sqrt{3}}{2}B_{TE}E_z & -\frac{1}{2}B_{TE}E_z & B_{TA}E_z \\ 0 & \frac{\sqrt{3}}{2}B_{TE}E_y & -\frac{\sqrt{3}}{2}B_{TE}E_z & 0 & 0 & 0 \\ B_{TE}E_x & -\frac{1}{2}B_{TE}E_y & -\frac{1}{2}B_{TE}E_z & 0 & 0 & 0 \\ B_{TA}E_x & B_{TA}E_y & B_{TA}E_z & 0 & 0 & 0 \end{pmatrix} \tag{A20}$$

where $\mathbf{E} = \mathbf{E}_{\rm ext}$ is the static E field due to *external* sources. Note that we have dropped the external field subscript here and in the remainder of the Appendix, in order to keep the expressions such as Eq. (A20) as compact as possible. To convert this matrix into an expression involving the applied E field, we would simply divide by ϵ_0 and replace the external field with the applied field wherever the external field occurs in this expression. The B_{TA} and B_{TE} coupling coefficients occurring in this equation can be determined easily by calculating the $A_{1g} - T_{1u}x$ and $E_g2 - T_{1u}x$ mode coupling for a [100] applied E field. In order to determine the splitting for the pocket *isotope* modes, we found it easiest to add the isotope mass perturbation to the static E-field coupling given by Eq. (A20) and then determined the effects of the applied E field upon the isotope mode by solving the full field plus mass perturbation problem.

From the form of Eq. (A20), we see that the first-order E-field-induced coupling cannot affect the isolated gap modes (no diagonal coupling). However, it can mix the nearly degenerate even- and odd-parity modes. Recall that the odd-parity modes are IR active, whereas the even-parity modes are Raman active (with predicted strengths too weak to be measured). Under the E-field induced mixing, the even-parity modes will acquire some odd-parity character and become E-field-induced IR active. If we assume that the applied E field does not alter the effective charges which

determine the absorption strengths for the IR-active gap modes, then the $\hat{x}$-polarized IR absorption strength for the ith mode determined from the nearly degenerate perturbation theory is given by[8]

$$S_i=\frac{2\pi^2 N}{cn(\omega_i)V}\left(\frac{n_\infty^2+2}{3}\right)^2[\tilde{\mathscr{M}}^x\boldsymbol{\chi}(T_{1u}x)]^2 a^2_{T_{1u}x}(i), \tag{A21}$$

where $n_\infty=\sqrt{\epsilon_\infty}$ is the high-frequency index of refraction and c is the speed of light in vacuum. The index of refraction, $n(\omega)$, is taken to have its pure-crystal value owing to our assumption of low defect concentrations. This expression is just the zero-field absorption strength multiplied by the $T_{1u}x$ fraction, $a^2_{T_{1u}x}(i)$, for the ith, isotope mode and by an index of refraction correction, $n(\omega_{T_{1u}})/n(\omega_i)$.[8] Hence, the relative $\hat{x}$-polarized IR absorption strengths for the E-field mixed modes are simply given by these $T_{1u}x$ fractions. Similar expressions exist for the $\hat{y}$- and $\hat{z}$-polarized IR absorption.

For the QD model, the first-order field-induced mixing is small and we have to consider higher-order effects, such as frequency shifts produced by force constant changes arising from second-order E-field-induced strains via cubic anharmonicity. Before discussing the second-order strains, we briefly mention the standard description of the quadratic Stark effect.[19] This second-order effect arises from force-constant changes produced by the first-order E-field-induced displacements via quartic anharmonicity, and it leads to E-field-induced force-constant changes that vary as $E^2_{\rm dc}$. The expression for these quartic anharmonicity second-order force-constant changes is

$$\delta\Phi^{Q2}_{\alpha\beta}(kl)=\frac{1}{2}\sum_{mn\gamma\lambda}\Phi_{\alpha\beta\gamma\lambda}(klmn)\xi^{(1)}_\gamma(m)\xi^{(1)}_\lambda(n), \tag{A22}$$

where the $\Phi_{\alpha\beta\gamma\lambda}(klmn)$ are the quartic anharmonic coefficients. Thus, this second-order Stark effect arises from quartic anharmonicity, as opposed to the cubic-cubic second-order Stark effect discussed below. Unfortunately, the second-order field-induced force-constant changes produced by the quartic anharmonicity lead to mode coupling which has the same symmetry form as the coupling produced by cubic-cubic coupling, so that the cubic-cubic and quartic anharmonicity effects cannot be separated on the basis of symmetry arguments.

The E-field-induced displacements linear in $E_{\rm dc}$ used in Eq. (A22) are the crystal's harmonic response to the applied field. Cubic anharmonic corrections to these harmonically determined E-field-induced displacements also produce field-induced force-constant changes proportional to $E^2_{\rm dc}$. In order to determine the second-order E-field-induced strains, we need to consider the anharmonic version of Eq. (A1), which determines the harmonic crystal response to an external force. The anharmonic generalization of this equation for the static case is

$$\sum_{m\beta}\Phi_{\alpha\beta}(nm)\xi_\beta(m)+\frac{1}{2}\sum_{m\beta l\gamma}\Phi_{\alpha\beta\gamma}(nml)\xi_\beta(m)\xi_\gamma(l)+\cdots = F_\alpha(n), \tag{A23}$$

where, as before, $\mathbf{F}$ is the external force and $\boldsymbol{\xi}$ is the static displacement induced by this force. Next, we formally expand the static displacements in orders, $\boldsymbol{\xi}=\boldsymbol{\xi}^{(1)}+\boldsymbol{\xi}^{(2)}+\cdots$, where $\boldsymbol{\xi}^{(1)}$ is the harmonic response and the higher-order terms are the corrections to this response produced by the presence of anharmonicity. To lowest order in the applied E field, Eq. (A23) is just the harmonic equation that we used previously to determine the first-order E-field-induced displacements:

$$\boldsymbol{\Phi}\boldsymbol{\xi}^{(1)}=\mathbf{F}. \tag{A24}$$

The second-order equation is

$$\sum_{m\beta}\Phi_{\alpha\beta}(nm)\xi^{(2)}_\beta(m) = -\frac{1}{2}\sum_{m\beta l\gamma}\Phi_{\alpha\beta\gamma}(nml)\xi^{(1)}_\beta(m)\xi^{(1)}_\gamma(l). \tag{A25}$$

Since the first-order displacements occurring on the right-hand side of this equation are linear in the E field, we see that the second-order displacements will be proportional to the E-field strength squared. An expression for these second-order displacements is easily obtained by multiplying Eq. (A25) on the left by the zero-frequency defect-lattice harmonic Green's function $\mathbf{G}(0)=\boldsymbol{\Phi}^{-1}$, which yields

$$\xi^{(2)}_\alpha(n)=-\frac{1}{2}\sum_{m\beta l\gamma k\lambda}G_{\alpha\beta}(nm)\Phi_{\beta\gamma\lambda}(mlk)\xi^{(1)}_\gamma(l)\xi^{(1)}_\lambda(k). \tag{A26}$$

It is convenient to map this problem formally onto the first-order displacement problem discussed earlier in Eqs. (A1)–(A5). We replace $\boldsymbol{\xi}^{(1)}$ appearing there by $\boldsymbol{\xi}^{(2)}$, $\boldsymbol{\xi}^{(1)}_0$ by $\boldsymbol{\xi}^{(2)}_0$, and $\{(\mathbf{F}_{\rm ext})_\alpha(n)\}$ by $\{-(1/2)\Sigma_{m\beta l\gamma}\Phi_{\alpha\beta\gamma}(nml)\xi^{(1)}_\beta(m)\xi^{(1)}_\gamma(l)\}$. This last term can be treated formally as an applied force, with $\boldsymbol{\xi}^{(2)}_0$ then giving the pure host-crystal response to this force. Expressing the problem this way allows us to calculate the second-order field-induced displacements via the same techniques used for calculating the previous first-order field-induced displacements.

Once the needed $\xi^{(2)}_\alpha(n)$ displacements are determined, we can calculate the lowest-order cubic-cubic E-field-induced force-constant changes by simply replacing the first-order displacements occurring in Eq. (A18) with the second-order E-field-induced displacements, which yields

$$\delta\Phi^{2CC}_{\alpha\beta}(lm)=\sum_{n\gamma}\Phi_{\alpha\beta\gamma}(lmn)\xi^{(2)}_\gamma(n), \tag{A27}$$

where the CC superscript labels these E-field-induced force-constant changes as cubic-cubic changes.

Equation (A26), which determines the second-order displacements, involves products of two first-order displacements which have T_{1u} symmetry. From standard group-theoretic arguments, analogous to those used in deriving selection rules,[51] the second-order displacements transform as the direct product $T_{1u}\times T_{1u}$. This direct product can be broken down uniquely into A_{1g}, E_g, and T_{2g} symmetry contributions, and hence the second-order displacements can also be broken down into displacements with these symmetries.

With the cubic-cubic coupling included, Eq. (A19), which determines the first-order E-field-induced frequency shifts, generalizes to

$$(\mathscr{B}_E+\mathscr{C}_E-\mathbf{\Delta}\omega^2)\mathbf{a}=0, \tag{A28}$$

where $\mathscr{B}_E$ is still the first-order coupling and $\mathscr{C}_{E,ff'}=\tilde{\boldsymbol{\chi}}(f)\,\delta\mathbf{\Phi}^{2CC}\boldsymbol{\chi}(f')$ is the 6×6 matrix giving the cubic-cubic coupling for the degenerate pocket modes. Using standard group-theoretic symmetry arguments, similar to those used to determine the first-order field-induced coupling, it can be shown that the matrix $\mathscr{C}_E$ coupling the pocket gap modes can be written in general as

$$\mathscr{C}_E=E^2\begin{pmatrix}\mathbf{C}_{\rm odd} & \mathbf{0}\\ \mathbf{0} & \mathbf{C}_{\rm even}\end{pmatrix},$$

where $E=|\mathbf{E}|$ is the magnitude of the E field due to external sources and the 3×3 matrices occurring in this expression are

$$\mathbf{C}_{\rm odd}=\begin{pmatrix} C_{E1}+2C_{E2}(2E_x^2-E_y^2-E_z^2)/E^2 & C_{E3}E_xE_y/E^2 & C_{E3}E_xE_z/E^2\\ C_{E3}E_xE_y/E^2 & C_{E1}+2C_{E2}(2E_y^2-E_x^2-E_z^2)/E^2 & C_{E3}E_yE_z/E^2\\ C_{E3}E_xE_z/E^2 & C_{E3}E_yE_z/E^2 & C_{E1}+2C_{E2}(2E_z^2-E_x^2-E_y^2)/E^2\end{pmatrix} \tag{A29}$$

and

$$\mathbf{C}_{\rm even}=\begin{pmatrix} C_{E4}+C_{E5}\epsilon & \sqrt{3}C_{E5}\rho & \sqrt{3}C_{E6}\rho\\ \sqrt{3}C_{E5}\rho & C_{E4}-C_{E5}\epsilon & C_{E6}\epsilon\\ \sqrt{3}C_{E6}\rho & C_{E6}\epsilon & C_{E7}\end{pmatrix}, \tag{A30}$$

with $\epsilon\equiv(2E_x^2-E_y^2-E_z^2)/E^2$ and $\rho\equiv(E_y^2-E_z^2)/E^2$. The second-order coupling coefficients occurring in Eqs. (A29) and (A30) can be determined by calculating the following matrix elements:

$$C_{E1}+4C_{E2}=\tilde{\boldsymbol{\chi}}(T_{1u}x)\,\delta\mathbf{\Phi}^{2CC}(E[100])\boldsymbol{\chi}(T_{1u}x)/E^2,$$

$$C_{E1}-2C_{E2}=\tilde{\boldsymbol{\chi}}(T_{1u}y)\,\delta\mathbf{\Phi}^{2CC}(E[100])\boldsymbol{\chi}(T_{1u}y)/E^2,$$

$$C_{E3}=2\tilde{\boldsymbol{\chi}}(T_{1u}x)\,\delta\mathbf{\Phi}^{2CC}(E[110])\boldsymbol{\chi}(T_{1u}y)/E^2,$$

$$C_{E4}+2C_{E5}=\tilde{\boldsymbol{\chi}}(E_g1)\,\delta\mathbf{\Phi}^{2CC}(E[100])\boldsymbol{\chi}(E_g1)/E^2,$$

$$C_{E4}-2C_{E5}=\tilde{\boldsymbol{\chi}}(E_g2)\,\delta\mathbf{\Phi}^{2CC}(E[100])\boldsymbol{\chi}(E_g2)/E^2,$$

$$2C_{E6}=\tilde{\boldsymbol{\chi}}(A_{1g})\,\delta\mathbf{\Phi}^{2CC}(E[100])\boldsymbol{\chi}(E_g2)/E^2,$$

$$C_{E7}=\tilde{\boldsymbol{\chi}}(A_{1g})\,\delta\mathbf{\Phi}^{2CC}(E[100])\boldsymbol{\chi}(A_{1g})/E^2,$$

where $\delta\mathbf{\Phi}^{2CC}(E[lmn])$ are the cubic-cubic force-constant changes induced by an external E field aligned along the $[lmn]$ direction.

In order to determine the splitting for the *isotope* pocket gap modes, we found it easiest to add the isotope mass perturbation to the static E-field coupling given by Eqs. (A20), (A29), and (A30) and then determine the effects of the applied E field upon the isotope mode by solving the full field plus mass perturbation problem.

*Present address: Naval Research Lab., Code 5611, Washington, D.C. 20375.

†Permanent address: Physics Dept., Simon Fraser University, Burnaby, BC, Canada.

[1] A. J. Sievers, Phys. Rev. Lett. **13**, 310 (1964).

[2] R. D. Kirby, I. G. Nolt, R. W. Alexander, and A. J. Sievers, Phys. Rev. **168**, 1057 (1968).

[3] I. G. Nolt and A. J. Sievers, Phys. Rev. **174**, 1004 (1968).

[4] R. D. Kirby, Phys. Rev. Lett. **26**, 512 (1971).

[5] R. D. Kirby, Phys. Rev. B **4**, 3557 (1971).

[6] A. J. Sievers and L. H. Greene, Phys. Rev. Lett. **52**, 1234 (1984).

[7] J. B. Page, J. T. McWhirter, A. J. Sievers, H. Fleurent, A. Bouwen, and D. Schoemaker, Phys. Rev. Lett. **63**, 1837 (1989).

[8] K. W. Sandusky, J. B. Page, A. Rosenberg, and A. J. Sievers, Phys. Rev. B **47**, 5731 (1993).

[9] S. B. Hearon and A. J. Sievers, Phys. Rev. B **30**, 4853 (1984).

[10] S. Takeno and A. J. Sievers, Phys. Rev. Lett. **15**, 1020 (1965).

[11] R. W. Alexander, A. E. Hughes, and A. J. Sievers, Phys. Rev. B **1**, 1563 (1970).

[12] N. W. Ashcroft and N. D. Mermin, *Solid State Physics* (Saunders College, Philadelphia, 1976).

[13] I. M. Lifshitz, Nuovo Cimento Suppl. **3**, 716 (1956).

[14] A. A. Maradudin, E. W. Montroll, G. H. Weiss, and I. P. Ipatova, *Theory of Lattice Dynamics in the Harmonic Approximation*, 2nd ed. (Academic, New York, 1971), Suppl. 3.

[15] H. Bilz, D. Strauch, and R. K. Wehner, *Handbuch der Physik* (Springer-Verlag, Berlin, 1984), Vol. XXV, Pt. 2d.

[16] A. Rosenberg, C. E. Mungan, A. J. Sievers, K. W. Sandusky, and J. B. Page, Phys. Rev. B **46**, 11 507 (1992).

[17] K. W. Sandusky, J. B. Page, A. Rosenberg, C. E. Mungan, and A. J. Sievers, Phys. Rev. Lett. **67**, 871 (1991).

[18] K. W. Sandusky, A. Rosenberg, B. P. Clayman, J. B. Page, and A. J. Sievers, Europhys. Lett. **27**, 401 (1994).

[19] A. S. Barker and A. J. Sievers, Rev. Mod. Phys. **47**, S1 (1975).

[20] J. B. Page (unpublished).

[21] K. Fischer, H. Bilz, R. Haberkorn, and W. Weber, Phys. Status Solidi B **54**, 285 (1972).

[22] K. Fischer, Phys. Status Solidi B **66**, 295 (1974).

[23] B. Dorner, W. v. d. Osten, and W. Bührer, J. Phys. C **9**, 723 (1976).

[24] W. G. Kleppmann, J. Phys. C **9**, 2285 (1976).

[25] H. Bilz, Cryst. Lattice Defects Amorph. Mater. **12**, 31 (1985).

[26] P. W. M. Jacobs, J. Imaging Sci. **34**, 79 (1990).
[27] J. Corish, J. Imaging Sci. **34**, 84 (1990).
[28] S. B. Hearon, Ph.D. thesis, Cornell University, 1986.
[29] B. P. Clayman, R. D. Kirby, and A. J. Sievers, Phys. Rev. B **3**, 1351 (1971).
[30] A. Rosenberg, Ph.D. thesis, Cornell University, 1993.
[31] B. P. Clayman and A. J. Sievers, Phys. Rev. Lett. **21**, 1453 (1968).
[32] R. D. Kirby and A. J. Sievers, Solid State Commun. **6**, 613 (1968).
[33] R. D. Kirby, A. E. Hughes, and A. J. Sievers, Phys. Rev. B **2**, 481 (1970).
[34] W. J. Shotts and A. J. Sievers, Phys. Rev. B **10**, 4495 (1974).
[35] W. J. Shotts, Ph.D. thesis, Cornell University, 1973.
[36] R. W. Ward and B. P. Clayman, Phys. Rev. B **9**, 4455 (1974).
[37] D. Baüerle and R. Hübner, Phys. Rev. B **2**, 4252 (1970).
[38] M. Born and K. Huang, *Dynamical Theory of Crystal Lattices* (Oxford University Press, Oxford, 1954).
[39] R. J. Elliott, J. A. Krumhansl, and T. H. Merrett, *Localized Excitations in Solids*, edited by R. F. Wallis (Plenum, New York, 1968), p. 709.
[40] U. Schröder, Solid State Commun. **4**, 347 (1966).
[41] W. G. Kleppmann and W. Weber, Phys. Rev. B **20**, 1669 (1979).
[42] M. Bucher, J. Imaging Sci. **34**, 89 (1990).
[43] S. Kapphan and F. Luty, Phys. Rev. B **6**, 1537 (1972).
[44] F. Bridges, Phys. Rev. B **5**, 3321 (1972).
[45] F. Bridges, CRC Crit. Rev. Solid State Sci. **5**, 1 (1975).
[46] U. Holland and F. Luty, Phys. Rev. B **19**, 4298 (1979).
[47] F. Bridges and D. Chow, Phys. Rev. Lett. **54**, 1532 (1985).
[48] F. Bridges and M. Jost, Phys. Rev. B **38**, 12 105 (1988).
[49] K. W. Sandusky, Ph.D. thesis, Arizona State University, 1994.
[50] J. B. Page and D. Strauch, Phys. Status Solidi **24**, 469 (1967).
[51] See, for instance, M. Tinkham, *Group Theory and Quantum Mechanics* (McGraw-Hill, New York, 1964), p. 80.